Experiments and prediction of the spreading behavior of fibrous tows by means of the Discrete Element Method

Master Thesis

Amir Ahmad Bakhtiary Davijani
June 2012

University of Twente
Faculty of Engineering Technology
Department of Mechanical Engineering
Chair of Production Technology

Graduation committee:

Prof. Dr. rer.-nat. S. Luding
Prof. Dr. ir. R. Akkerman
ir. B. Cornelissen
Dr. T. Weinhart

Summary

A single tow consists of thousands of filaments which are bundled together and may be used as it is or further processed and woven into a fabric. Due to its discrete nature the tow shape can significantly change under loading. The shape of the tow can have an impact on several production and performance aspects. For instance, tow deformation can influence the permeability of a fabric during resin impregnation. It can also affect the dimensions and thickness of products, for example in braiding or filament winding processes.

This study is focused on modeling the spreading behavior of continuous fiber materials or tows. Several experiments were designed to identify the most relevant deformation mechanisms and measure their effect. During the experiments it was determined that the main mechanisms playing a role in tow spread are the setup geometry, sizing and twist and within the range of measurements friction and tow tension had no significant effect. After the identification of the spreading mechanisms, they were implemented using a discrete element approach. The Discrete Element Method was used to predict the tow spread, shape and structure by modeling the individual filaments of the tow. Various simplifications were made to start with the most simple model. Subsequently other features were implemented to understand their importance one-by-one. The discrete element method also provided the possibility of analyzing stress and pressure in the tow packing. Comparison of the experimental and numerical results concluded that DEM is a suitable tool for modeling tow deformation. The model can predict the effect of setup geometry and the presence of sizing well within 10 percent of the experimental results.

Contents

Nomenclature

Symbol	Description
d	Free tow (or filament) length
h	Height or y component of free tow (or filament) length d
z	Component of free tow length, d, in the z-direction (or filament)
z_c	Clamp to center of spreader bar distance
a	Filament radius
h_p	Filament height
f	Force per unit length
F	Force
σ	Stress
k	Particle Stiffness
γ	Dissipation Coefficient
b	Virtual damping Coefficient
ϵ	Coefficient of Restitution
m	Particle mass
a	Particle radius
N	Number of particles
t_c	Collision time
δ	Overlap
s	cohesion factor
x	Lateral or x-component of length d of the filament
w	Spread of the tow
R	Radius of spreader bar
L	Total length of the tow (or filament)
E	Elasticity modulus of material
T	Tension
l^{pc}	Branch vector

Chapter 1

Introduction

Composite materials are widely used in modern industry nowadays, in fact one can say that Fiber Reinforced Plastics (FRP) have made a revolution in manufacturing. Structures which were previously impossible or expensive to manufacture are now easily made. One of the main advantages of FRPs is the high strength and stiffness to weight ratio. This characteristic allows composite materials to be used in places were weight is a limiting factor while high strength is required, for instance in aircraft and aerospace industries. The application of these materials has extended to automotive, civil, sport equipment and many other applications.

1.1   Background

The main disadvantage of composite materials was the high cost of labor and materials and the slow production time compared to other conventional materials. Since most of the manufacturing was carried out by hand labor the quality of the final product was highly operator dependent and repeatability was not satisfactory. As time passed more advanced materials and manufacturing methods were introduced; automation reduced costs of labor and production time while increasing equipment cost. A more important impact of automation of manufacturing was increased product quality removing the operator dependence of quality. However, it was crucial to be able to control the manufacturing process carefully to obtain the desired structure with the best performance.

Fiber reinforced composites are materials made of two or more constituent materials, being a matrix and a reinforcement. The matrix is usually a thermoplastic or thermoset polymer (resin) and the reinforcement can be any type of tow material. The tows are usually glass, carbon or aramid, although other types of materials, such as natural fibers, can be used. The tows are available in various forms, such as continuous, short or chopped threads. Each tow consists of several thousands of filaments which are wound together to make the tow (fig. 1.1).

The performance of these materials depends on the behavior of each constituent and the interaction between them as a whole. There are many issues to be considered during production of a composite structure based on the type of manufacturing method. In general, the matrix should be continuous throughout the structure with no voids, optimal adhesion should exist between the matrix and fiber surface, alignment of the fibers should
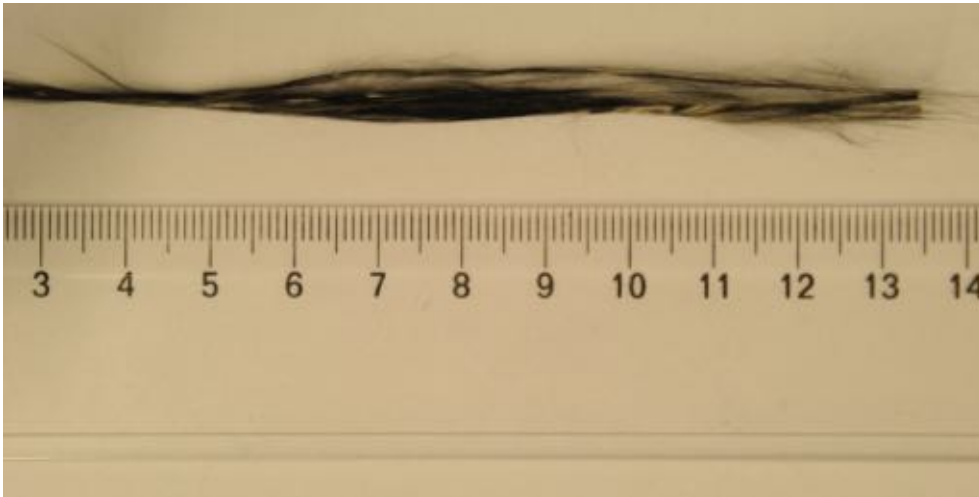
Figure 1.1: Sample tow specimen.

be controlled, resin rich areas should be avoided and automation of the process should be possible.

Any type of dry spot or area with bubbles will be a suitable location for stress concentration, hence crack initiation and growth. For instance in vacuum infusion, it is crucial to prevent the creation of voids and dry spots and obtain the required thickness. To reduce adverse effects and obtain the perfect structure many parameters such as vacuum pressure, temperature, resin mix, amount of resin and many other have to be controlled [1–4].

Another parameter is the fiber alignment. Although fibers and tows have high strength and stiffness under tension, due to their natural flexibility they cannot tolerate compressive forces. During production the fibers can move under different forces, such as the viscous force exerted by the flow of resin or compression of the layers which may lead to undesirable fiber orientation and waviness [5, 6]. Many studies have shown the adverse effect of fiber waviness on ultimate stiffness and strength [7–10].

In compression molding, the molding material is placed in a mold and formed to the desired shape. Compression molding is a high volume method which can be used to manufacture complex and strong fiber reinforcements. However, if not carried out correctly, the material can tear or wrinkle leading to the decrease of strength and stiffness. Many studies have been conducted to characterize and control adverse effects such as wrinkling in this production method [11–13].
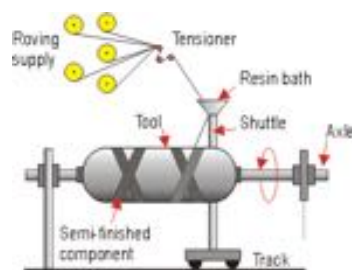

Figure 1.2: Schematic setup of filament winding.

Controlling the dimensions of the product is also important. In filament winding, after impregnation, the tows are wound around a mandrel (mold core) in a controlled pattern to form the shape of the mandrel (fig. 1.2). As the fiber tow is wound over the mandrel it will spread under tension and flatten out up to some degree, which depends on how the winding process is done. In braiding, the deformation of the filaments will have an impact on the thickness of the end product and on resin rich areas.
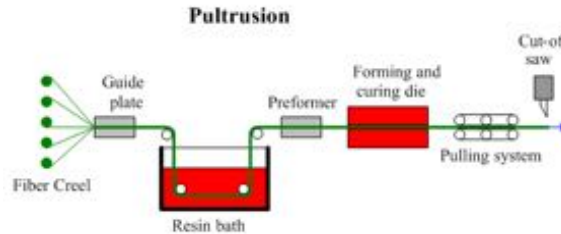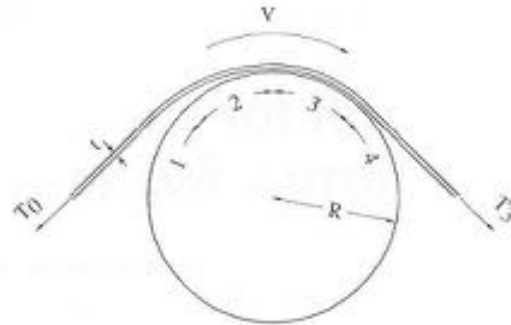

Figure 1.3: Schematic of the pultrusion process.

Figure 1.4: The four zones defined by Chandler et al. around the spreader bar [14].

It is also desirable to obtain good adhesion between the matrix and fibers. This requires that the resin adequately wets the fiber surface. In several processes, such as pultrusion (fig. 1.3), the tow is pulled through a resin bath before being formed into a final product. In the resin bath, the tow is pulled over a set of spreader bars to deform the tow in a way to facilitate the spreading which in turn improves the penetration of resin, or impregnation. As the tow passes through the resin bath it should, ideally, become completely saturated. Chandler et al. [14] modeled the impregnation process, based on the lubrication theory, during which a tow is pulled over a spreader bar, similar to what is done in a pultrusion process. Four zones were defined on the spreader bar in this model with different conditions as shown in (fig. 1.4). The required length for full impregnation and the tension build-up was calculated analytically and compared with experimental values. The experimental values were in the range of the model. However, the parameters related to the shape of the tow were chosen to obtain the best fit between the experiments and model. While it is clear that the tow shape will have an impact on the impregnation process. It has been shown that resin penetrates the tow much easier when spreader bars are used compared to not using spreader bars [15]. As the tow passes over the bars it spreads and flattens out which helps the wetting process. In one study, the process was

optimized using the Taguchi method [16], considering several parameters such as pull speed, melt temperature, number of pins and pretension, which concluded in optimized values. However, as more spreader bars are used, the tension in the tow increases, which is required to be kept to a minimum due to residual stress in the final product. Also high stresses may lead to a failure in the filaments of the tow. Therefore it is necessary to optimize the number of spreader bars to control this effect while achieving acceptable impregnation. Several studies have been conducted on this issue.

The focus of this study is predicting the spreading behavior of tows using a new approach.

1.2   Motivation

A single tow consists of thousands of filaments which are bundled together and may be used as it is or further processed and woven into a fabric. Due to its discrete nature the tow shape can significantly change under loading. The shape of the tow can have an impact on several production and performance aspects. For instance, tow deformation can influence the permeability of a fabric during resin impregnation. It can also affect the dimensions and thickness of products, for example in braiding or filament winding processes.
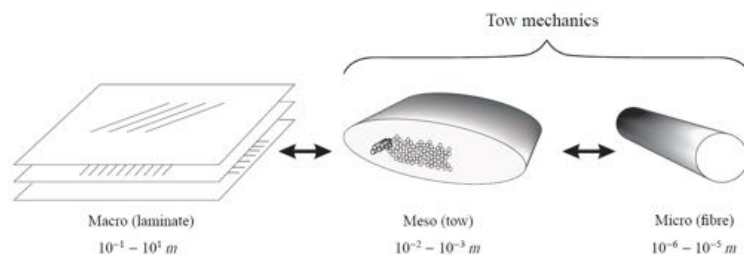
Figure 1.5: Macro-micro-meso structure of composite materials [17].

The tows make up a laminate and consecutively the laminates make up the structure (fig. 1.5). Therefore, the deformation of a tow is important since it affects the final dimensions of a laminate. It is vital to understand the effect of different forces and conditions on the deformation of tows.

Another issue is how contact forces are distributed in tows during manufacturing processes. For example, in braiding, weaving and other production processes the tow is guided through rings. As the tow deforms and the filaments are pressed together, the pressure and stress on each filament may cause the filaments to fail, which in turn can disrupt the production process or reduce the final quality of the product. Continuum modeling of the tow does not allow considering pressure and stress inhomogeneity between the filaments.

1.3 Objective

Considering the issues stated above, it would be very helpful if the tow deformation could be modeled more precisely under different load conditions. In this master thesis, the aim is to model this behavior using the Discrete Element Method (DEM). In addition to providing a suitable tool for predicting tow spreading, it can provide more insight into general tow deformation, which can be very helpful in many production processes. It may also provide better understanding of pressure and stress distribution and evolution, issues which cannot be easily modeled when the tow is considered as a continuum.

1.3.1 Discrete Element Method

The Discrete Element Method (DEM), is a type of numerical method for computing the motion of a number of particles on the micro, meso or larger scale. The beauty of DEM is its simplicity. With advances in computing power and numerical algorithms for nearest neighbor sorting, it has become possible to numerically simulate millions of particles on a single processor. An important tool in modeling the mechanical behavior of granular assemblies, DEM was developed in the 70s by Cundall and Strack [18]. It is a numerical model where the motion of all particles, usually disks in 2D and spheres in 3D or any arbitrary particle, is determined for every time step.

Today DEM is becoming widely accepted as an effective method of addressing engineering problems in granular and discontinuous materials, especially in granular flows, powder mechanics, and rock mechanics. Even though simple, Discrete Element Methods are relatively computationally intensive, which limits either the length of a simulation or the number of particles.

1.4 Organization of thesis

A brief literature review on tow deformation is given in chapter 2. The experimental aspects of this study, such as the experimental setup, materials and results of the measurements, is presented in chapter 3. Chapter 4 is dedicated to the modeling section of the thesis, where the basic foundation of the DEM model is explained. The model will start from a simplified version and a feature will be added in each step and compared with the simplified model. Afterwards a final model with the relevant features is implemented. In chapter 5, the experimental and numerical results will be compared and recommendations for future research will be given.

Chapter 2

Literature on tow deformation

Tow deformation is critical throughout many fiber reinforced material production processes. Different methods and approaches have been used to model tow deformation. Most studies have modeled tows and fabric yarns as a continuum to investigate the deformation and impact response of fabrics made of these tows [19–26]. Only a few studies have gone into the detail of modeling the tow as an assembly of smaller filaments. The most common fundamental study on this topic is Wilson's approach [27], which will be introduced in detail in the next section.

2.1 Wilson's model

A theoretical treatment of lateral spreading of the filaments was proposed by Wilson [27]. Wilson treated the filaments in the bundle as a continuum and derived an expression for the width of the bundle at the spreader bar.
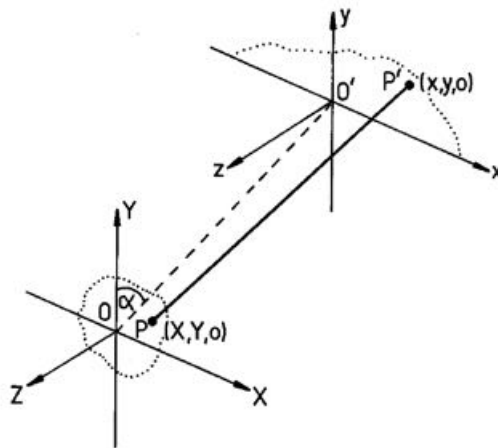

Figure 2.1: The tow is gripped at O and is pulled over a spreader bar, which is modeled as a thin blade and where $O'x$ is the upper edge of the cylinder, and the tow is gathered symmetrically at the other side of the bar. PP' represents a filament [27].
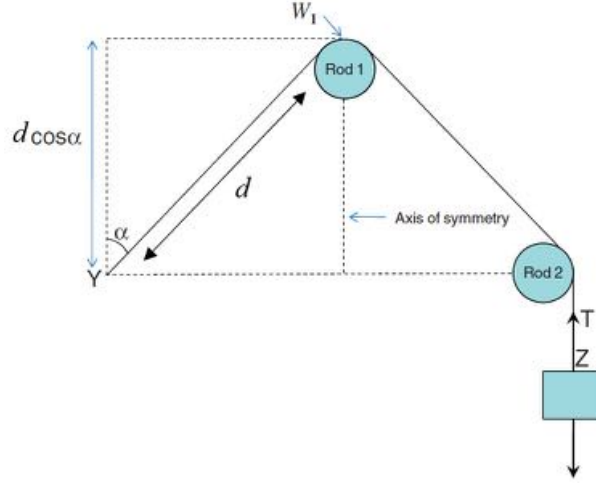
Figure 2.2: Schematic side view illustration of Wilson's experiment [28].

Wilson proposed a simplified analytical approach to predict tow deformation. A symmetrical one bar configuration was considered as shown in fig. 2.1. The filament bundle is held at O with an initial shape and is pulled over a spreader bar and is gathered symmetrically on the other side. Two coordinate systems were defined to simplify the problem, coordinate system XYZ with origin at O and coordinate system xyz with origin O'. The planes OXY and $O'xy$ are parallel and $|\overrightarrow{OO'}| = d$. A filament goes from point P in the OXY plane to point P' in the $O'xy$ plane. The filament PP' can be defined using the vector:

$$PP' = (x - X, y - Y + d\cos\alpha, -d\sin\alpha). \tag{2.1}$$

The length of the filament is $d = |\overrightarrow{PP'}|$. The filament is pulled with force T from both sides. The components of the forces at P' can be easily calculated. The x-component is $2T(X - x)/d$ and the y-component is $2T(Y - y - d\cos\alpha)/d$. Wilson assumed that the tension is constant throughout the filaments and also neglected friction. After making several assumptions due to the dimensions of the problem, the tension resultants are thought to be balanced by a hydrostatic pressure $p(x, y)$ satisfying:

$$\frac{\partial p}{\partial x} = \frac{2Tn}{dl}(X - x), \tag{2.2}$$

$$\frac{\partial p}{\partial y} = \frac{2Tn}{dl}(-d\cos\alpha + (Y - y)\sin^2\alpha), \tag{2.3}$$

where n is the number of filaments per unit cross-section area and l is the distance in the z direction over which the tension acts on the bar. in order to obtain the pressure p, the equation should be dimensionless. The scale for X and Y has been assumed a. An auxiliary term ϵ, which is small, has been defined as:

$$\epsilon = (a/d)^{1/3} \tag{2.4}$$

and by considering the orders of magnitude, $x \sim a/\epsilon$ and $y \sim a\epsilon$ and the scale for p is $2Tna\epsilon/l$ and also the cross section of the tow which is constant is equal to one. Applying these values to make eq. (2.2) and eq. (2.3) dimensionless:

8

$$\frac{\partial p}{\partial x} = -x + \epsilon X \tag{2.5}$$

$$\frac{\partial p}{\partial x} = -\cos\alpha + \epsilon^3 Y \sin^2\alpha - \epsilon^4 \sin^2\alpha \tag{2.6}$$

If the small terms are neglected the pressure p can be obtained:

$$p = -\frac{1}{2}x^2 - y\cos\alpha + const = -\frac{1}{2}x^2 - y\cos\alpha + \frac{1}{2}c^2 \tag{2.7}$$

On the outer boundary of the tow, the pressure is zero, $p = 0$, and $y = y_s(x)$ where $y_s(x)$ is the shape of the free surface:

$$y_s(x)\cos\alpha = \frac{1}{2}(c^2 - x^2) \tag{2.8}$$

The constant c can be found by requiring that the total cross section area equals one:

$$c = \left(\frac{3}{2}\cos\alpha\right)^{\frac{1}{3}} \tag{2.9}$$

The width of the tow is $w = 2c$. Translating (2.9) back into physical values gives back the total width of the tow:

$$w = (12\cos\alpha d a^2)^{\frac{1}{3}} = (12Ah)^{\frac{1}{3}} \tag{2.10}$$

where A is the tow cross section and h is the height or y-component of length d, $h = d\cos\alpha$.

The general trend of theory and experiments appeared well in Wilson's study. However, there was 15% difference between his predictions and experiments, which was attributed to neglecting friction and the natural entanglement or twist of the filaments. In addition to these assumptions, Wilson makes further assumptions to translate the dimensions of the equations. One outcome of these simplification is that the lateral height, h, is the only geometrical dependency of the setup on the tow width in Wilson's approach. This means that if height, h, is kept constant, the theoretical spread width remains the same and is independent of the tow length d. The experiments Wilson conducted were very limited. Generally multiple spreader bars are required to achieve desirable level of impregnation [29]. Irfan et al. [28] extended Wilson's approach to predict the width, thickness and profile of the bundle at the second spreader bar. They also conducted several experiments, examining several parameters such as the bar diameter, tow length, angle α and number of bars and compared those with Wilson's approach. The measurements were carried out under different tension conditions and they exceeded Wilson's estimates from 10% to 30% based on different conditions. In their study, in one case the effect of tow length, is examined while the angle α is kept constant. As expected, since $d\cos\alpha$, is increased the width increases. It seems there should also be a correlation with the tow length d. Therefore, the predicted tow spread should change when d and α are changed in a way that $d\cos\alpha$ remains constant, while theory predicts otherwise; the tow width remains constant in theory.
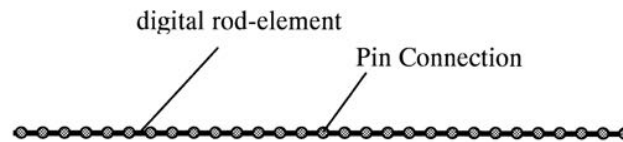
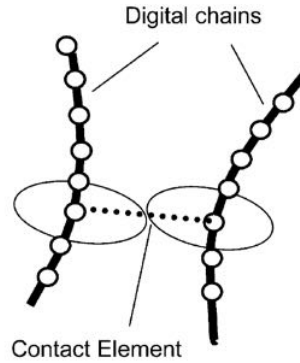Figure 2.3: Discretization of one filament or tow [30].

Figure 2.4: Digital chains and contact elements [31].

2.2 Numerical methods

There are other studies which have used commercial FEM software or developed their own software to model tow deformation. The FEM method was used to model the deformation and mechanical properties of braided and woven fabrics [32, 33].
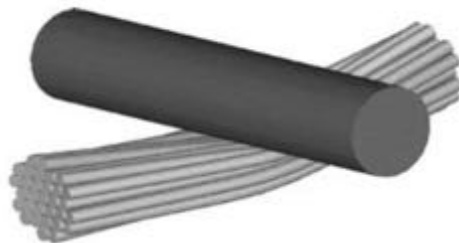
Figure 2.5: Tow deformation under compression using digital elements [31].

In another study a procedure, similar to finite element analysis, was adopted. A digital-element model was developed by Wang and Sun to simulate textile processes and determine the micro-geometry of textile fabrics [30]. It models tows by a pin-connected digital-rod-element chain. As the element length approaches zero, the chain becomes fully flexible, imitating the behavior of tows (figure 2.3). Zhou et al. [31] developed a finite element model based on the digital element model concept established by Wang and Sun. They used a finite number of digital chains (<100) to represent filaments in a bundle, rather than tows, and predicted tow geometry in woven fabrics using contact mechanics. Contact between digital chains was modeled by contact elements (2.4). Displacement of filaments inside a fabric was derived based upon the global stiffness matrix and the boundary conditions. An example of a deformed tow using this method is shown in figure

2.5. The multi-chain digital element approach was used for the simulation of the two-dimensional weaving and three-dimensional braiding processes. The yarn cross-section shape inside the woven and braided fabric can be viewed section by section. The numerical results were not compared to other methods or experiments. This model was also used to simulate the impact and penetration of textiles [34], which corresponded well with experimental results. However, they have not used this model to study its ability in predicting tow deformation and to compare it with experiments.

2.3 Overview

Although Wilson does provide a quick prediction for tow spread, it seems that his model fails to take many aspects of the deformation into account. In this study, a discrete element model is implemented for this problem. Hopefully, with this model more realistic factors of the deformation can be considered. The result of the two approaches will be compared with each other and with the experiments to verify the applicability of the two methods.

Chapter 3

Experimental

Knowledge of tow deformation can help in many composite production processes as discussed in the introduction. It may prevent rich resin areas from occurring, help determine the thickness of fiber reinforced structures and improve the resin impregnation process. There are only few experimental studies on tow deformation. These studies focused on relating the experimental analysis to an analytical approach [12, 27, 28]. This chapter explains the experimental aspects of this study, lays out the procedure for obtaining results and presents the results. The purpose of the experiments is to first identify the important mechanisms in tow spreading and also to obtain the spread of the filaments, the width of the spread tow, under specific loading conditions. The results will be used to verify the numerical results obtained in chapter 4. First the materials are introduced in section 3.1, then the experimental setup and the experimental procedure are explained in section 3.2. Finally, the results are presented and the mechanisms which affect the tow deformation are discussed in section 3.3.

3.1   Materials

The tow consists of several thousands of filaments which are bundled together. The tow material used in this study are T300J, produced by TORAYCA. The properties of the material provided by the manufacturer are summarized in table 3.1. The material was obtained in two forms, with sizing and without sizing. Since TORAYCA only provides the material with sizing (sized), the sizing was removed by TenCate under a thermal decomposition process (desized). The sizing was epoxy based.

Sizings and finishes are a mixture of chemical compounds applied to the tow material to protect the surface (e.g. coupling agent for glass fibers) and aid in handling (e.g. binder, lubricant, antistatic agent). In order to remove the sizing the material undergoes a chemical or thermal process. It should be noted that the filaments are easily damaged when the sizing is removed.

Filament Diameter

An important characteristic of the tow material which may influence the model is the polydispersity of the filament diameter. Only the mean of the filament diameter was provided by the manufacturer. In order to measure this distribution, a short tow specimen

Table 3.1: Torayca T300J carbon fibre tow properties provided by the supplier

Fiber properties	Value	Units
Filament diameter	7	μm
Tensile modulus	230	GPa
Tensile Strength	4210	MPa
Density	1.78	g/cm^3
Elongation	1.8	%
Number of Filaments	3000	-
Cross Sectional Area	0.11	mm^2

was spread out manually and mounted on the sample holder. The filaments were examined using Scanning Electron Microscopy (SEM) (fig. 3.1). The radii of twenty filaments were measured to obtain the mean and standard deviation of the diameter distribution. The mean measured diameter was 6.99 μm and the standard deviation was 0.0956 μm with a standard error of 0.0219. These statistical data are used in Chapter 3, to simulate polydispersity in the model.
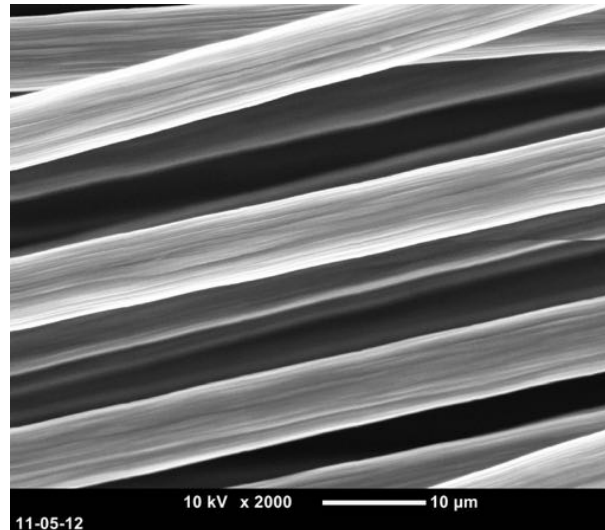
Figure 3.1: SEM picture of carbon filaments to obtain statistical values of the filament diameter distribution.

3.2 Tow spreading Setup

The experimental setup of this study is straightforward and simple. In order to study the spreading behavior of the tow, the tow is pulled over three bars and the width or spread of the tow on the middle bar is measured (fig. 3.2). The bars on the side are identical hence the setup is symmetric. Identical weights are attached to both ends of the tow and they are left hanging as shown in fig. 3.2. The tows are tied to the weight holders. The free length of the tow hanging from each side is at least 15 cm.

Figure 3.2: Left: The two side bars and the main middle spreader bar of the setup, note that the setup is symmetric around the center bar, the notch in the side bars are visible. Right: The setup as a whole with the tow tied to the weights.

One particular issue is controlling the boundary conditions. The tow should be kept bundled together at the side bars to prevent the spread at those locations since it will affect the boundary conditions. For this purpose two identical bars were machined with a small notch to guide the tow and prevent it from spreading. The notched bars can be seen in fig. 3.2 (left). The notch prevents the tow from spreading at the side bars.

When the tow is mounted it spreads to some extent, but this is not the balanced spread. The tow must undergo several tension cycles, until it reaches an equilibrium degree of fiber spreading. Each tension cycle consists of pulling the weight of one side down vertically and allowing the tow to move over the spreader bar. Then the procedure is repeated on the other weight and then it is returned to the original position. Due to friction at the side bars some filaments which are in contact with these bars will experience negative strain. To prevent this the weights are gently pulled down to completely tension the tow after the tension cycles. Irfan et al. [28] determined that the tow specimen they used required six tension cycles to achieve the equilibrium. In this study, the sized tow specimens required five tension cycles, while the desized tow specimens required only one tension cycle to reach the equilibrium spread.

After achieving the equilibrium spread, an optical microscope was used to measure the tow spread at the center spreading bar. The calibration procedure of the microscope is explained in detail in Appendix A. The measurements were carried out using 4x magnification.

A typical measurement of spread is shown in fig. 3.3. To obtain the width of the spread the number of pixels from side to side is obtained and is multiplied by the length per pixel. In this case the width of the tow is 2.09 mm. Due to resolution restraints the edge cannot be exactly distinguished, which can lead to error. The edge selection error is less than 12 pixels, therefore for the 4x zoom this would lead to an error of $\pm$ 0.01 mm.
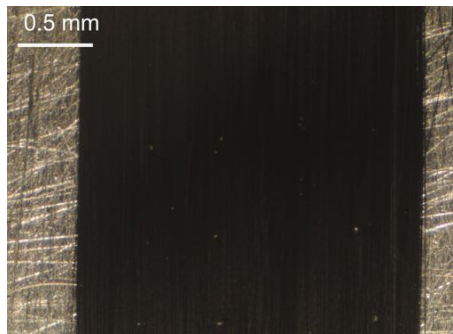
Figure 3.3: Typical measurement of a desized tow specimen spread over an aluminium bar, h=20 mm and β=12.1 degrees, 4x zoom.

3.2.1 Geometry and Details of the Setup

The experiments were carried out for different geometries and distances. The relevant distances are shown in fig. 3.4. The diameters of the side bars are neglected and assumed to be very small. The distance from the center of the bar to where the tow is bundled at the side bar is z_c, the radius of the center bar is R, the length of the tow without contact is d , and h and z are the y-component and z-component of the free tow length d, respectively. For the experiments, first z_c is kept constant while h, therefore also β, is increased. Note that increasing h will reduce z. These measurements are also carried out for different z_c. For the central spreader bar, two types of material were used, a steel bar with radius $R = 3$ mm and two aluminium bars with radii $R = 3$ mm and R=15 mm. After the bars were machined to obtain the desirable dimensions, they were polished with 1200 grit sandpaper, in the direction parallel to the axis of the cylinders. The most common surface roughness parameters of the three bars are shown in table 3.2. Before mounting the tow on the setup the surface of the spreader bar was cleaned with acetone and then ethanol to remove dust and fat.

Table 3.2: Roughness parameters of the three spreader bars.

Spreader bar	S_a (μm)	S_q (μm)
Aluminium R=15 mm	0.384	0.463
Aluminium R=3 mm	0.493	0.551
Steel R=3 mm	0.231	0.311

Boundary Conditions

The boundary conditions dictate the forces applied to the filaments. Being able to completely control the boundary conditions is complicated, and hence simplifications should be considered. As much as the experimental procedure is concerned, there are several issues such as how the tow is attached to the weight, the effect of the contact of the tow with the side bars and the total length of the tow. In this case the tow was attached to the weights by tying a knot to the weight and the length of the tow hanging was 15 cm on each side. With hope, it can be considered that the boundary condition is far away
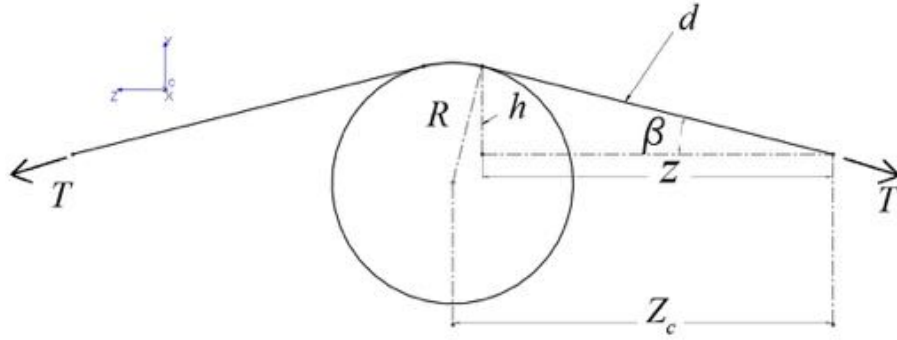
Figure 3.4: The geometry of the setup and the relevant distances.

enough not to affect the measurement of spread at the spreader bar. In order to verify this, the tow was clamped using clamps instead of tying a knot and also the hanging length of the tow was increased from 15 cm. No variation in spread was observed with these changes. Considering this, it should be safe to say that the tow deformation at the center is only affected by the side bars. Friction forces at the side bars were neglected.

3.2.2 Experiment parameter variation

A short summary of the experimental parameters are presented in table 3.3. In all experiments, desized tow specimens were used, the tow was without twist and the weight (or applied tension) was 200 g, unless specified otherwise. The code name of the steel bar with radius R=3 mm is S3 and the aluminium bars with radii R=3 mm and R=15 mm are Al3 and Al15, respectively. The procedure for applying these variations is explained in the following section.

Table 3.3: Summary of the parameter variations

Variation	$z_c(mm)$	h (mm)	Bar	No.[a]	Remarks
Twist	96.2	10	Al3	4	Twists of 0, 10.1, 30.4 twists per meter
Friction	96.2	10	S3,Al3	4	PTFE and graphite powder applied to Al3
Sizing	96.2	5,10,20,30	Al3	5	With and without sizing
Tow tension	96.2	5,10,20,30	Al3	4	200, 400, 600 g weight
Geometry	35,96.2	5,10,20,30	Al3,Al15	6	

a: Number of measurements or sample size.

Tow twist

Twist can occur in two forms, global twist and intra tow twist. Global twist can be prevented and resolved to some extent. This can be done by holding one end of the tow and allowing the tow to unwind itself. One possibility is to apply a global twist manually and measure the effect of the twist on the spread. This was carried out for a typical tow

spread measurement. The tow was manually twisted and the spread was measured and compared to the spread of an untwisted tow under the same conditions. A tow with a length of 490 mm was twisted manually with five and fifteen complete rotations, which is equivalent to 10.1 and 30.4 twists per meter, respectively. Identifying intra tow twist is somewhat less straight forward than global twist. While some filaments may be parallel, most filaments are probably displaced in the tow and cause twist in the structure of the tow.

Friction variation

The tow spread was measured under three different frictional conditions in addition to the normal condition. The bar and tow surface were treated prior to the tow spread measurement. Graphite powder was used in one and PTFE spray in the other measurement. PTFE Spray is a lubricant and anti adhesive medium for hygienical dry lubrication. Both PTFE and graphite powder are used to reduce friction. Also measurements were carried out using a steel spreader bar with diameter of 6 mm.

Tow specimen sizing

As stated previously the tow is provided in two forms, with and without sizing. The sizing significantly prevents the filaments from spreading, which is probably caused by an increased cohesion between the filaments or in other words causing them to stick together. Experiments are carried out with the sized and desized tow specimens with different geometries.

Tension variation

In order to vary tension, several dead weights were used. The measurements were carried out with weights of 200, 400 and 600 grams on each side. When higher weights were used filament damage became very severe so that the measured values were not consistent, especially since the desized specimens are vulnerable to damage.

Geometry variation

The location of the side bars, z_c, and the height of the center bar was varied. In addition to that two spreader bars with different radii were used.

3.3   Results and Discussion

In order to extract the tow deformation behavior and the factors and mechanism which have the most impact, several measurements were carried out under different conditions. The result for the following variations will be presented in this section.

- Twist of the tow

- Friction

- Tow sizing

- Tow tension

- Effect of the geometry

3.3.1 Results

The results are briefly presented here and discussed in the following section. The plots are provided with error bars which indicate the standard deviation of the measurements.
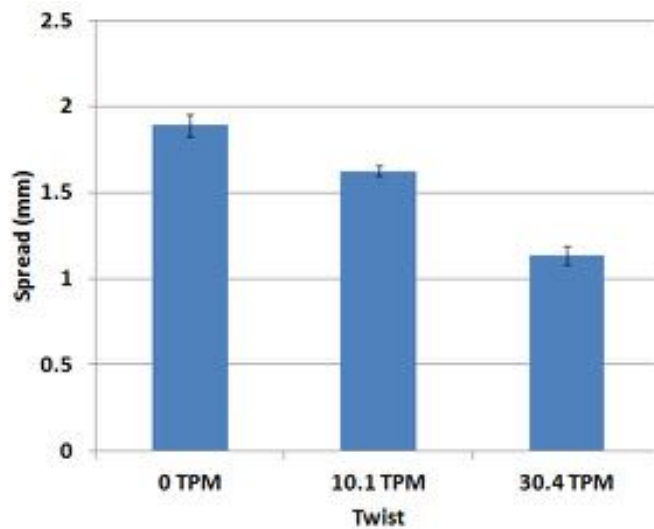

Figure 3.5: Spread of the tow with different degrees of twist.
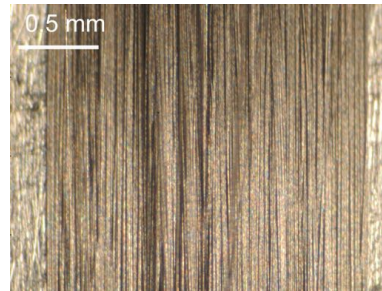

Figure 3.6: Spread of untwisted, desized tow

The results of the spread are shown in fig. 3.5 for different degrees of twist. An example of the three twist conditions are shown in fig. 3.6, fig. 3.7 and fig. 3.8 which are with 0, 10.1 and 30.4 twists per meter, respectively. When the original tow was used without twist the average spread of the tow was measured to be 1.89 mm. However, when five rotations were applied to the tow the spread was reduced to 1.63 mm. The twist is not very evident from fig. 3.7, however, the spread has been reduced by about 15 percent. When fifteen rotations were applied to the tow, the spread reduced to 1.14 mm. The twist is evident from the microscopic image, since the filaments are not oriented straightly.
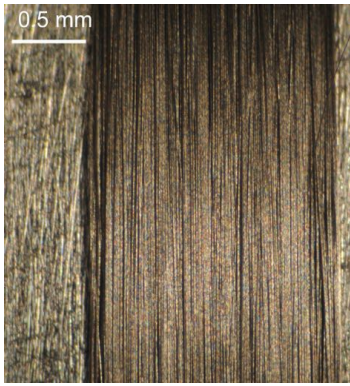
Figure 3.7: Spread of twisted, desized tow with 5 complete rotations, 10.1 twists per meter.
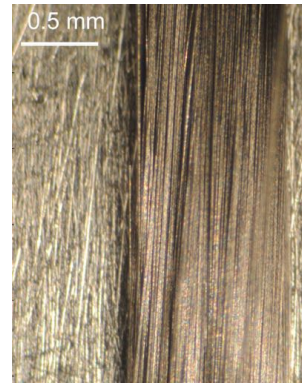

Figure 3.8: Spread of twisted, desized tow with 15 complete rotations, 30.4 twists per meter.

The results for the friction variation is shown in fig. 3.9 and the spread of the sized and desized tow specimen is plotted in fig. 3.10. The measurements using different weights is presented in fig. 3.11 and the effect of geometrical aspects is shown in fig. 3.12.
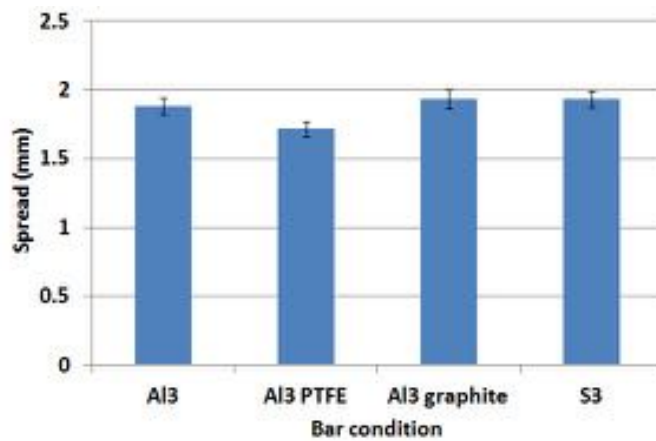

Figure 3.9: Tow Spread under different surface conditions.

3.3.2 Discussion

In order to better model the deformation of the tow, it is crucial to identify the main mechanisms which play a role in deformation and spread of the tow. These mechanisms dictate how the forces are applied on the filaments and hence the final shape of the tow. The main mechanism which are discussed are the geometry of the setup, twist, friction, sizing, tow tension and boundary conditions.

Mechanisms governing deformation

As pointed out in this chapter, several mechanisms play a role in tow deformation. Some mechanism were found to play little or no role in tow deformation. It was determined that
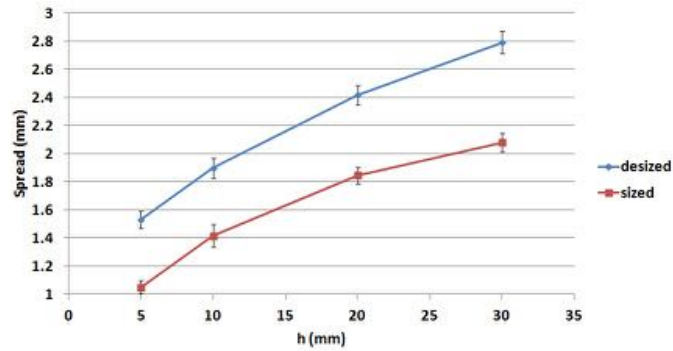
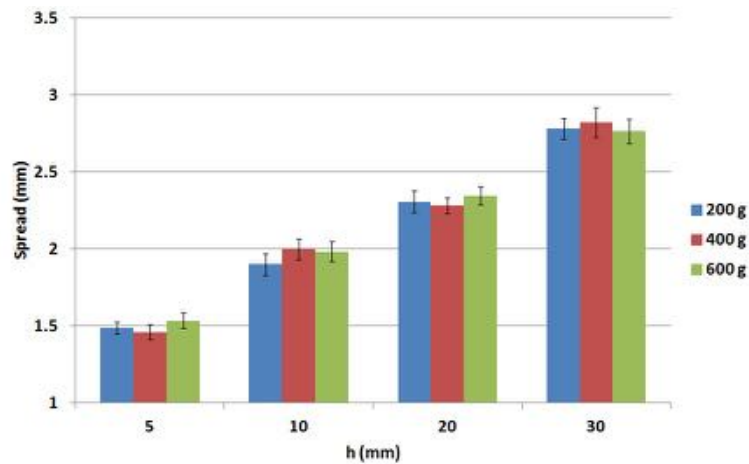Figure 3.10: Effect of sizing on the tow spread.

Figure 3.11: Spread as a function of tension using three different weights, or under three different tension conditions.

tow spread is independent of the tow tension in the tested tension range. Considering the materials and lubricants used in this study, no dependency was observed regarding the effect of friction on tow deformation. In order to make a better judgement several types of material with different roughness should be used to confirm the independence of tow spread of friction.

On the other hand several parameters displayed strong variations on tow spread. Twist may greatly influence tow deformation depending on the amount of twist. Sizing also plays an important role in tow deformation. By keeping the filaments together sizing significantly reduces spread. The geometrical aspects of the setup were yet another important factor. It was observed that tow spread can be maximized by reducing the spreader bar diameter and increasing the tension gradient in the tow.

Twist

The results of the tow spread under different twist conditions (fig. 3.5) clearly show the effect of twist on tow deformation. As expected twist prevents the filaments from spreading. Since the tow is twisted the filaments are bundled together. Depending on the amount of twist, twist will have an effect similar to shortening the tow. The normal
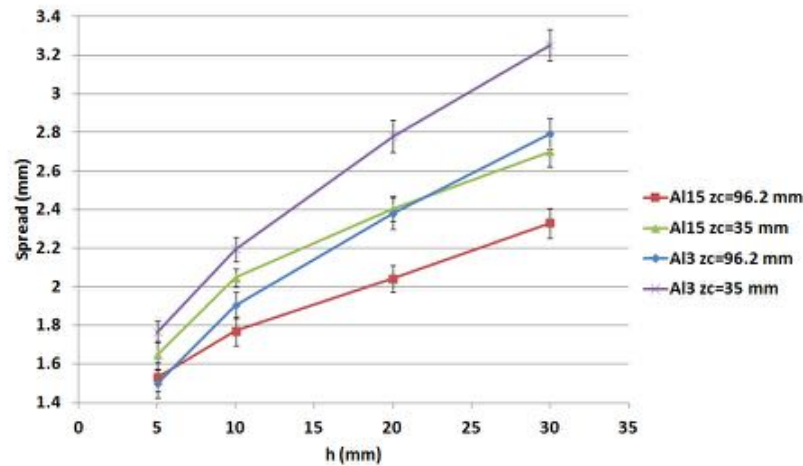
21

Figure 3.12: Tow spread under different geometrical conditions, with aluminium spreader bars with $R=3$ mm and $R=15$mm.

component pressing the filaments down stays constant while the lateral force holding the tow together increases. The purpose of discussing twist is not to quantify the effect of twist but to give an approximation of its effect. Dire care should be taken when handling the tow before measurement to prevent twist.

Friction

As in all mechanical systems friction is present and will inevitably affect the final deformation and spread of the tow. Two types of friction exist, the friction between the surface of the bar and the filaments, and the friction between the filaments themselves. The friction between the surface and the tow is dictated by the roughness and the material of the spreader bar. Comparing the spread using the different spreader bars in fig. 3.9, the small difference between the two can be neglected considering the error bars. However, when PTFE spray was applied to the aluminium bar and tow surface, tow spread reduced. This is probably due to the capillary effect of the spray, since it was oil based. As the lubricant particles penetrate and wet the filaments, it builds up adhesion, which in turn keeps the filaments together. When graphite powder was applied to the surface no significant change was observed in tow spread. The outcome was that the measured spread was similar for the original condition without using lubricants and with using lubricants. Although, deriving a solid conclusion is very difficult from this observation, but two possibilities exist. Either these lubricants did not have any effect on friction or the friction was already low and the lubricants could not further reduce it, or the spread of the tow is independent of friction altogether.

Sizing

Sizing significantly reduced the tow spread as shown in fig. 3.10. The spread of the tow is 26 to 33 percent higher for the desized tow compared to the sized tow. The sizing increases cohesion between the filaments causing them to stick together, therefore reducing spread.

Obviously, if a sizing with higher stickiness and binding effect is used, the spread of the tow would decrease even further.

Tension

Considering the effect of tension on tow spread, the results are within close range for the three weights which were used (fig. 3.11) and do not follow a specific trend and the variations are not significant. Hence it can be assumed that the spread is indeed independent of the applied tow tension in the range of the applied weights.

Although, if a larger range of tension is tested, some trend may be observed. The results will be more accurate if the side bars and the spreader bars are free to rotate, to reduce friction at those locations.

Geometry

One of the most important aspects of the experiments was studying the effect of geometry on tow deformation. The tow deformation for four different geometrical conditions is shown in fig. 3.12. The general trend is that as height h increases the spread increases. This is due to the fact that the normal component which forces the filaments down goes higher.

First the effect of spreader bar diameter is discussed. At constant horizontal clamp distance, z_c, for a smaller spreader bar diameter, the spread is larger. Therefore if the spreader bar has an infinitesimally small size the tow spread is expected to increase. This can be explained by considering how the forces are applied on the filaments. The normal force component is equal for the small and large spreader bar. However, the normal force per unit length is different for different sizes. The normal force per unit length, f_n is derived in section 4.2 as:

$$f_n = \frac{T_i}{R} \tag{3.1}$$

where T_i is the tension applied on filament i. It is clear that as R increases, f_n is reduced. This means that the normal force is applied on a longer length. This may be the possible explanation for the difference, since the load distribution varies with the two conditions. It should be noted that since the DEM model only predicts the deformation of one cross section it is favorable to conduct the experiments with a small as possible spreader bar.

The second observation can be made when the result of similar spreader bars with different z_c are considered, when z_c is reduced, the spread increases. As z_c is reduced the normal load component increases, however, at the same time the lateral force component, preventing spread and holding the tow together, also increases to the same extent (this is explained thoroughly in Chapter 4). From this, it is expected that the spread remains constant. However, as z_c is reduced, the contact angle 2β increases. The filaments at the bottom close to the bar surface have lower tension compared to the filaments stacked on them. This is due to the fact that the bottom filaments are less strained compared to the filaments at the top of the tow. Two filaments in a tow are shown in fig. 4.10. From the figure it is clear that as β increases the upper filament will experience higher strain compared to the lower filament. This will cause a gradient in the tension of the filaments based on where it is located. This gradient increases as β grows. Since the filaments on
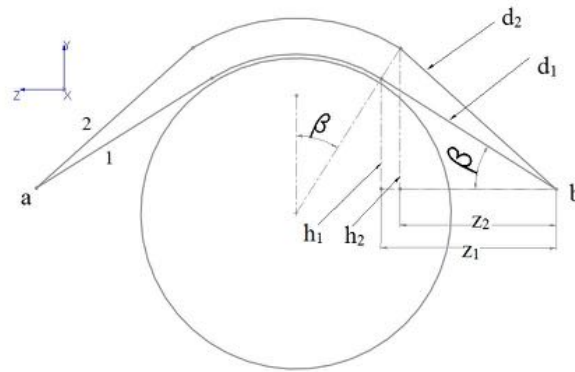
Figure 3.13: Two filaments are gripped at points a and b. The stacking has been exaggerated.

the top, have a higher tension, they will push down further causing the tow to spread. As they move down their strain is reduced and the tension gradient becomes smaller. The filaments which spread sideways are also strained which prevents excess spread up to some extent. The strain dependent behavior is discussed thoroughly in section 4.3.1.

3.4   Summary

In this chapter, the experimental side of this study was discussed. After introducing the setup, different experiments were designed to study the effect of different parameters on tow spread. In the tested range, no observable influence was observed regarding friction and tow tension. However, twist, sizing and geometry were found to have a strong influence. Twisting the tow and the addition of sizing reduce tow spread.

Chapter 4

Discrete Element Method

This chapter introduces the basics of the Discrete Element Method (DEM) and presents a model to characterize the deformation behavior of a tow cross-section. A tow consists of several thousand filaments which are bundled together. In order to predict the spreading behavior of the filaments using DEM, it is necessary to determine several parameters and the model's level of complexity. Several conditions can be considered and assumptions be made, each with various levels of simplification. In this study, a two dimensional approach is used in which one cross section of the tow will be modeled. An example of a tow cross section is shown in fig. 4.1. In the DEM model the particles represent the circular filaments in the figure.
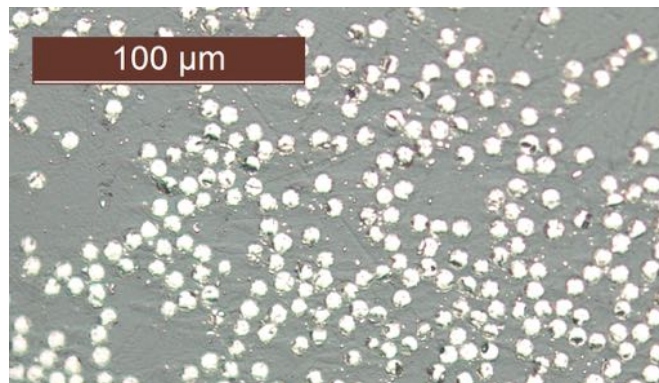

Figure 4.1: Microscopic image of a tow cross section. The bright circles are the filaments which are round. Imperfections are due to the polishing process, were the filament edges were chipped off.

First, the fundamentals and necessary parameters of a DEM model will be explained in section 4.1. Afterwards, a simplified model which corresponds with the experiment will be devised in section 4.2. Subsequently, additional features, such as strain dependence of tension, polydispersity and cohesion are added to the model and the effect of these features are discussed in section 4.3. Continuum quantities such as stress and pressure will be explained in section 4.4 and some continuum fields will be extracted and plotted for one setup. Finally, in section 4.6, a model which includes all relevant features will be implemented for comparison with experiments.

4.1 Introduction to DEM

A DEM simulation consists of a system of n particles with an initial position and velocity. At each time step the force on each particle is calculated. The most prevalent and important forces are those arising from collision, gravity, friction or other body forces applied to the particles. All of the forces are added up to obtain the total force on each particle. In every time step, the acceleration, velocity and position of each particle is obtained using Newton's equation of motion:

$$m_i \ddot{\vec{r}}_i = \vec{F}_i \tag{4.1}$$

where m_i is the mass of particle i with position $\vec{r}_i$ and acceleration $\ddot{\vec{r}}_i$ and subject to force $\vec{F}_i$. The new positions and velocities are calculated for the next time step and the process is repeated. However, the time step must be chosen carefully to satisfy some conditions, which will be discussed shortly.

4.1.1 Physical interpretation

In reality when two particles, in this case filaments, are pressed together, they deform and their surfaces flatten (fig. 4.2 a). If the deformation is elastic, the two particles will repel each other, exerting an opposing force on the center of mass of the particles. In order to calculate the exact deformation, intensive formulation of stress and strain relations must be carried out. Since it is difficult and computationally expensive to model the deformation of the contact an alternative method is used in DEM in which the particles are allowed to penetrate each other, repelling each other as they overlap (fig. 4.2 b).
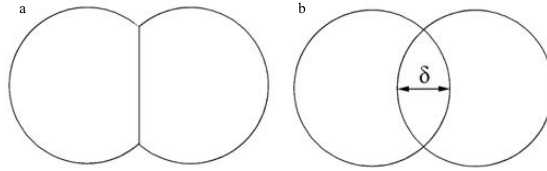

Figure 4.2: Schematic graphs of a) how the particles deform in reality, b) particle overlap in DEM

Two particles i and j, with diameter d_i and d_j, respectively, interact only when they are in contact so that their overlap $\delta = \frac{1}{2}(d_i + d_j) - (\vec{r}_i - \vec{r}_j).\vec{n}$ is positive, with the position vector $\vec{r}_i$ of particle i and the unit vector $\vec{n} = (\vec{r}_i - \vec{r}_j)/|\vec{r}_i - \vec{r}_j|$ that points from j to i (fig. 4.3). The symbol '.' denotes the scalar product of vectors.

There are several contact models that can be used to relate the contact force to the overlap. In this study a linear spring-dashpot model [35–37] is used to give the contact force, $\vec{F}_{ij}^{\,c} = \vec{F}_{n,\mathrm{el}} + \vec{F}_{n,\mathrm{diss}}$, exerted from particle j to particle i, which is consisted of an elastic and a dissipative term.

The repelling force depends on the overlap, δ, and a spring constant, k, representing the stiffness of the particles. The elastic force $\vec{F}_{n,\mathrm{el}}$ is written as:

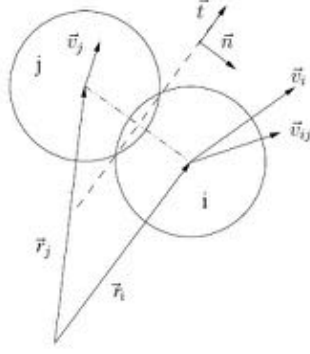$$\vec{F}_{n,\mathrm{el}} = k\delta\vec{n} \tag{4.2}$$

Figure 4.3: Definitions and distances of particles i and j used for the description of the force laws

One of the key features of granular materials is the dissipation of energy due to inter-particle collisions i.e. the transfer of kinetic energy into internal degrees of freedom of a particle and finally into heat. In order to introduce dissipation into the system, one assumes a viscous damping proportional to the relative velocity in the normal direction:

$$\overrightarrow{F}_{n,\text{diss}} = \gamma \overrightarrow{v} \tag{4.3}$$

where γ is the damping constant and $\overrightarrow{v} = -(\overrightarrow{v}_{ij}.\overrightarrow{n})\overrightarrow{n} = -((\overrightarrow{v}_i - \overrightarrow{v}_j).\overrightarrow{n})\overrightarrow{n}$.

The dissipation is quantified by the coefficient of restitution ϵ which is defined as the ratio of the post-collissional velocity, v^f (final), to the pre-collisional velocity, v^s (start), in a head on collision between two particles i and j:

$$\epsilon = \frac{v_i^f - v_j^f}{v_j^s - v_i^s} \tag{4.4}$$

The coefficient of restitution can also be written as:

$$\epsilon = exp\left(-\frac{t_c \gamma}{2m_{ij}}\right) \tag{4.5}$$

where $m_{ij} = m_i m_j / (m_i + mj)$ is the reduced mass. Note that eq. (4.4) and eq. (4.5) give the same results. The coefficient of restitution equals 0 for a completely inelastic collision and becomes 1 for a perfectly elastic collision. This can be easily verified by simulating the evolution of one particle. The coefficient of restitution can be obtained by dividing the two subsequent positive and negative peak velocities.

This model is analogous to inserting a spring and dashpot between the particles. The contact force exerted on particle j from particle i is similar but in the opposite direction, $\overrightarrow{F}_{ji} = -\overrightarrow{F}_{ij}$. Note that the stiffness and damping coefficient of all particles are similar. This model is known as the Kelvin-Voigt model in materials science. Other forces such as, body forces arising from the continuity of the tow, can be added to these forces.
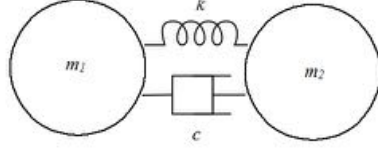
27

Figure 4.4: Linear spring-dashpot model

Virtual Damping

Usually in DEM simulation the particles are enclosed by boundary conditions or walls. In this study, the particles are only restricted from one direction and the particles are free to move in other directions. When the simulation starts, the particles scatter very quickly due to high kinetic energy. As the kinetic energy is damped out, the filaments regather and bundle up together again. This not only increases the simulation time, but alters the final solution of the problem, since when the fibers gather they will not achieve the statically balanced condition. The static condition can be achieved by causing a small disturbance to the system of particles, which will cause the particles to restructure.

It is favorable that the particles spread out by shear banding rather than scattering. The microscopic mechanism of shear banding has been extensively studied [38–41]. Considering these, a virtual viscous damping, $\overrightarrow{F}^b$ is also applied to the particles, $\overrightarrow{F}_i = \overrightarrow{F}^b_i + \overrightarrow{F}^c_{ij}$. The virtual damping force, $\overrightarrow{F}^b$, which is applied to each particle separately is defined as:

$$\overrightarrow{F}^b_i = -b.\overrightarrow{\dot{r}}_i \tag{4.6}$$

where b is the virtual damping coefficient and $\overrightarrow{\dot{r}}_i$ is the velocity of particle i.

Initially the model does not include friction. Altering this virtual damping will have an effect on the final solution. Hence, it can be assumed that this viscous effect can mimic dynamic friction to some accuracy. The main difference between friction and damping is that friction brings the system of particles to a stop while viscous damping reduces the kinetic energy but does not completely stop the evolution of the structure. If it is required to remove the damping, for instance for purpose of adding friction, the virtual viscous damping can be applied and when the particles are bundled together at the wall, b can be set to zero. Also note that the virtual damping further reduces the coefficient of restitution.

4.1.2   Time-step optimization

An important aspect of DEM simulations is to choose a correct time step. Choosing a large time step will lead to errors that will cause the energy of the system to increase irrationally and will cause the solution to 'explode'. When the time step is chosen too small, the simulation has to run for a too long time to obtain reasonable results. Therefore, the time-step should be optimized. For this purpose the contact time of a collision is considered and as a principle, in order to accurately describe the collision, approximately 50 time
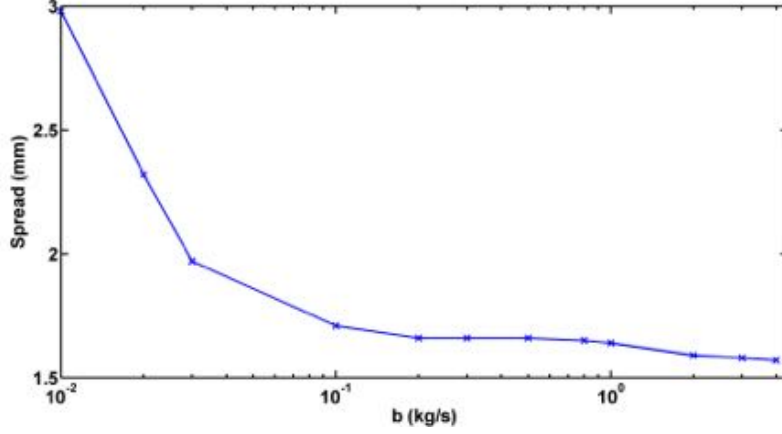
Figure 4.5: The effect of virtual viscous damping on the final spread, $n = 500$, $h = 10$ mm, $\beta = 6$ degrees, k=10 kg/s^2, γ=1 kg/s.
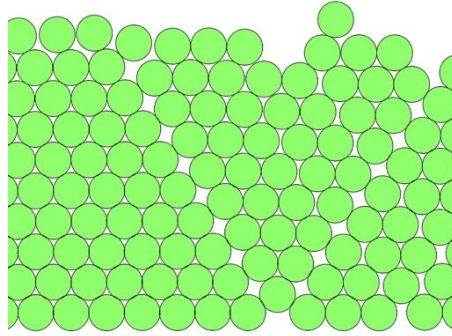

Figure 4.6: Deformation of particles by shear banding during the evolution of structure.

steps are required from the instance they come into contact until they separate [36]. The contact time of a collision is described by:

$$t_c = \frac{\pi}{\omega} \tag{4.7}$$

where ω is the natural frequency of the contact. The natural frequency of an under-damped system is a function of the natural frequency and the damping ratio.

$$\omega = \sqrt{\frac{2k}{m} - \zeta^2} \tag{4.8}$$

where k is the stiffness and ζ is the rescaled damping coefficient, $\zeta = \gamma/m$. In order to verify that eq. (4.8) is correct, two particles are pressed together and allowed to oscillate while in permanent contact. From the simulation results (time from peak to peak) the frequency can be obtained which should be equal to eq. (4.8).

From this, the selected time step is:

$$\Delta t \approx \frac{t_c}{50} \tag{4.9}$$

29

Since the simulation would run continue for further time steps, also an end condition must be defined when the simulation can stop.

4.1.3 Stability condition

In order to determine when the simulation has ended a criterion or a set of criteria must be defined. In this case the simulation is considered complete when the particles do not move anymore and have become stable. Several criteria can be defined in this case [42,43]. One criteria which is used often is the ratio of kinetic to potential energy. When this ratio falls below a predetermined amount, the simulation can be considered finished and that no considerable evolution will take place anymore.

The evolution of the solution, which is the spread of the particles, and its energy ratio is plotted in fig. 4.7. The evolution stopped after the energy ratio dropped below 10^{-3} after which no significant evolution took place in the structure. The used ratio in this study is 10^{-5}. In order to prevent the simulation from stopping at local values the average of this ratio should remain below the cut off value for the last 5000 time steps.
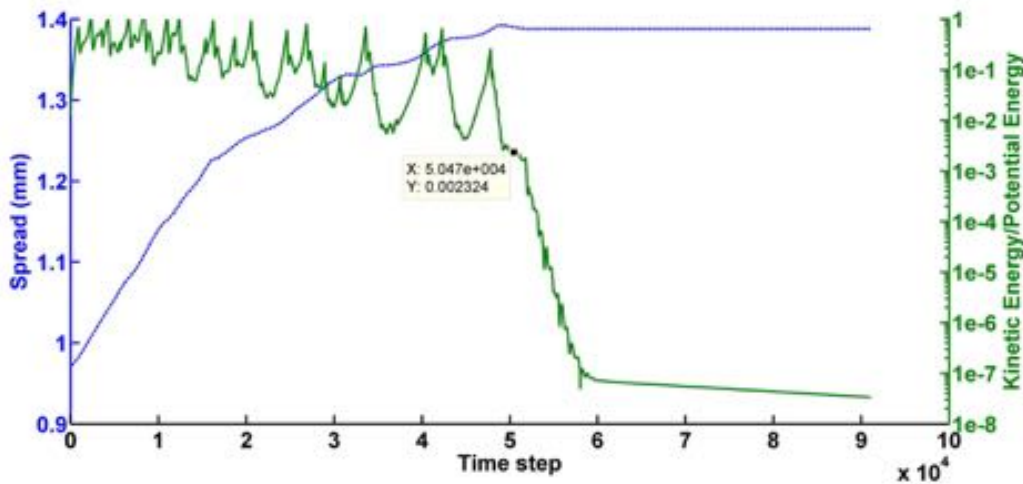

Figure 4.7: The spread of the particles and the energy ratio plotted together as a function of time step.

4.1.4 Particle Properties

The DEM model does not have a unit system. Therefore it is critical to ensure that chosen units are consistent. The fundamental units for this research are:

- Mass m_u, specified in kg

- Length x_u specified in m

- Time t_u specified in s

Occasionally, input algorithmic parameters that belong to dynamic simulations (e.g., damping, fictitious mass) are assigned values without any physical or mathematical justification, in some instances with the sole purpose of attaining a steady-state or quasi-static solution. One could argue that computational expense and spurious parameter calibration have prevented the method from penetrating practice further. In the case of computational expense, it is expected that full-scale computations using DEM will be possible in the next twenty years [44]. Since the dynamics of the problem are not the goal of this study and the final solution is static, fictitious values are assigned to the parameters. To obtain actual values these parameters should be scaled accordingly.

Table 4.1: DEM parameters, symbols and typical values

Parameter name	Symbol	Dimensionless Value	SI unit
Particle mass	m	1	kg
Particle radius	a	0.0000086	m
Particle Stiffness	k	10	kg/s^2
Viscous dissipation	γ	1	kg/s
Virtual damping*	b	0.1	kg/s
Coefficient of Restitution	ϵ	0.57	-
Number of particles	N	500	-
Collision time	t_c	0.721	s
Modulus of elasticity	E	230	$kg/(ms^2)$

* fictional parameter.

Typical values assigned to these parameters are presented in table 4.1. If it is required to use another value other than that stated in table 4.1 it will be indicated separately wherever required.

The justification for the specific particle radius a, is that since a typical tow used in the experiments has 3000 filaments with an average diameter of 7 μm and the simulation consists of 500 particles, the radius of the particles is chosen in a way that $\sum_{i=0}^{500} \pi a^2 = \sum_{i=0}^{3000} \pi (\frac{7}{2})^2$.

4.2   Simplified Model

In this section, the applied loads in the experiments are extracted and translated to the DEM model. Initially a simple model is developed and the results for this model is presented. In the next steps, several of the neglected features are introduced to make the model more realistic, and the effect of these variations are discussed. The simplified model assumptions are as follows:

- Constant tension on all filaments

- The contact length and contact angle is small and the spread is constant on the contact length, i.e. one cross section is sufficient

31

- Friction is neglected

- Filaments are clamped at a single point and there is no twist

- All filaments have the same radius (monodisperse particles)

4.2.1 Geometry

The geometry of the problem is critical due to the fact that it will determine how the forces are exerted on the particles. Since the cross section of the tow is modeled and the tow is continuous, forces arising from the tow continuity are applied to the filaments. The filaments, which are in contact with the spreader bar, will be modeled as cylindrical elements with radius a and height h_p and the forces will be applied to these elements.
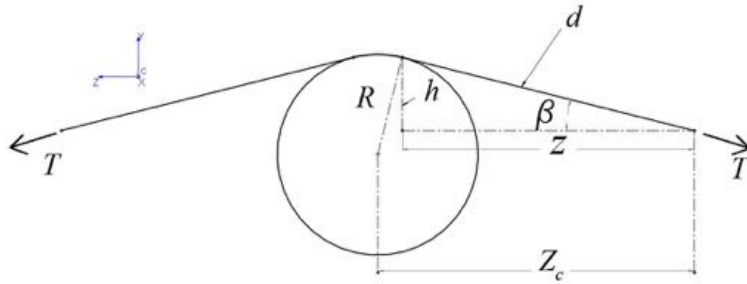

Figure 4.8: Side view of the experiment setup showing the geometry and the relevant distances used in the model.

In this setup a single tow consisting of n filaments is pulled over a spreader bar with radius R and makes an angle β with the horizontal, as shown in figure fig. 4.8. The distance of the clamp to the center of the spreader bar is z_c. The filaments converge to one point at length d where they are fixed at that point. Note that d is the length of the tow from where it leaves the spreader bar to the clamp and h and z are the $y-$ and z-components of d, respectively. The tow is pulled from both ends with force T and the wrap or contact angle of the tow over the spreader bar is 2β. First a small contact angle will be modeled where $2\beta \ll \pi$. As the tow is pulled over the bar, a normal component is introduced, pressing the filaments against the bar forcing them to spread. The boundary condition of the tow will constrain the tow, preventing the filaments from leaving the bar in the y-direction or spreading in the x-components. Therefore, there is a force on the filaments forcing them to spread and there is a force preventing spread which will allow for force equilibrium solutions. In the following, the forces acting on the filaments are determined.

4.2.2 Tensional Force

The tow is pulled over the bar with tension T from both ends. The friction between the tow and the bar is neglected, therefore tension is constant throughout the length of the tow. The simplest assumption is to consider that the tension on the tow is distributed evenly between all filaments. Therefore the tension on each filament will be $T_i = T/n$.

The tension introduces a normal and lateral component. These components are acting on each filament cross section individually.

4.2.3 Normal force

When the tow is tensioned over the spreader bar, a normal component presses the tow against the bar causing the tow filaments to spread. The larger the normal component becomes, the more the tow is expected to spread.
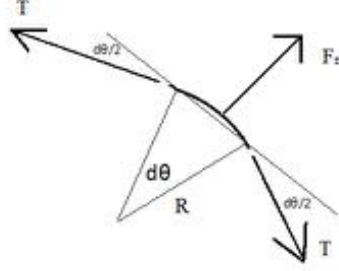

Figure 4.9: An infinitesimally small section of contact with normal force F_n.

An infinitesimally small section of the contact of one filament is shown in fig. 4.9. From the load balance in the normal direction we have:

$$F_n = 2T_i \sin\left(\frac{d\theta}{2}\right) \approx 2T_i \frac{d\theta}{2} = T_i d\theta \tag{4.10}$$

The length of this infinitesimally small filament is:

$$dl = Rd\theta \tag{4.11}$$

From this, the normal force on a unit length of this filament is:

$$f_n = \frac{F_n}{dl} = \frac{T_i d\theta}{Rd\theta} = \frac{T_i}{R} \tag{4.12}$$

Note that lower case f is used for the normal force per unit length. This shows that the normal force on a unit length of a filament is independent of the wrapping angle and only depends on the radius of the bar, R, and tension T for small values of θ. The normal and lateral forces exerted on filament segments of length dl should be analogous to one another. This means that if the normal force per unit length is used, for the lateral force, the force per unit length should be used too, as shown below.

4.2.4 Forces applied in DEM model

Initially the filaments are clamped at a single point as shown in fig. 4.10 and the fibers converge to a single point. Two filaments are shown in the figure. Filament 1 is closer to the bar surface while filament 2 is further away due to the stacking. Note that the tow can also displace laterally in the x direction as shown in fig. 4.11. The force components are separated since small angles and decoupling are assumed. In order to obtain the normal

and lateral forces applied to each filament, tension, T, should be decomposed to its $x-$ and y-components. The y-component of the tension for filament 1 is $-Th_1/d_1$. Since it is applied from both sides, the normal force on the surface becomes:

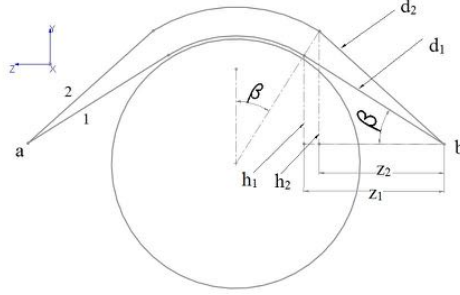$$F_n = -2T\frac{h_1}{d_1} \tag{4.13}$$

Figure 4.10: Two filaments are gripped at points a and b. The stacking has been exaggerated.

The length d_i of any filament can be obtained since the x, y and z-components are known, $d_i = \sqrt{x_i^2 + y_i^2 + z_i^2}$. Since filament 2 has different y-component and length, the normal force component will differ for that filament.
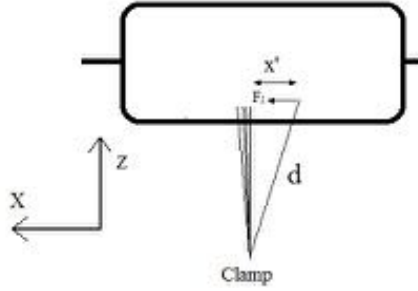

Figure 4.11: Top view of the setup displaying filament spreading.

Without a force to keep the tow together the particles can freely move away from each other and completely spread out on the surface. The main force holding them together is that of the boundary condition. As a filament spreads out an x-component force is introduced which prevents it from further spreading. The x-component or lateral component is:

$$F_l = -2T\frac{x_i'}{d_i} \tag{4.14}$$

As shown in fig. 4.11, x' is the lateral deflection distance from the clamp.

4.2.5 Initialization

An initial condition is required for starting the simulation. For these simulations it is considered that the tow is bundled together in a circular form as show in fig. 4.12. Initially

only a few bottom filaments are touching the lower wall. The simulation is started with a small height h and large virtual damping v_d to prevent chaotic movement of the filaments. This will cause the filaments to gently move down and rest on the lower wall. When the filaments come to rest and the kinetic energy is damped out, this condition (fig. 4.13) will be used as an initial condition for the simulations. In each step of the simulation h is incremented and the resulting spread is recorded. After each increment the final results are used as an initial condition for the next increment. So the end result for the simulation where h=5 mm is the initial condition for the simulation where h=10 mm. This will reduce simulation time and will help achieve shear banding, the preferred way of structure change (section 4.1.1).
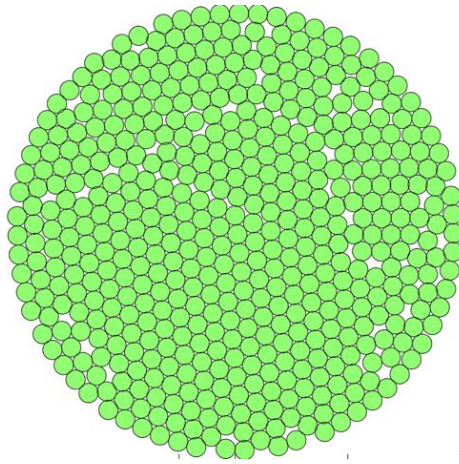

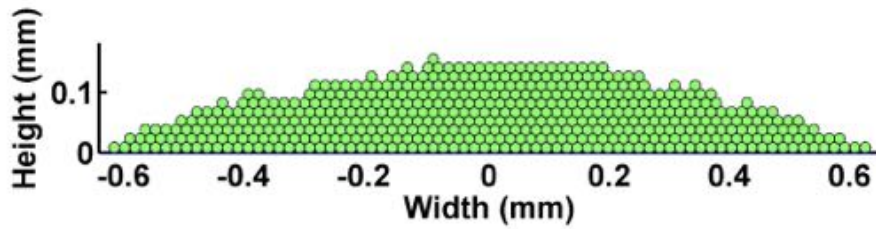Figure 4.12: Initial circular condition of the filaments.

Figure 4.13: Filaments rested on the surface used as the initial condition.

Example

A system of particles is modeled as an example. The resulting spread of the particle system is shown in fig. 4.14 when $h = 5$ mm and $\beta = 3°$. The spread width of the tow, w, is determined as the distance from the far left particle to the far right particle plus the diameter of one particle.
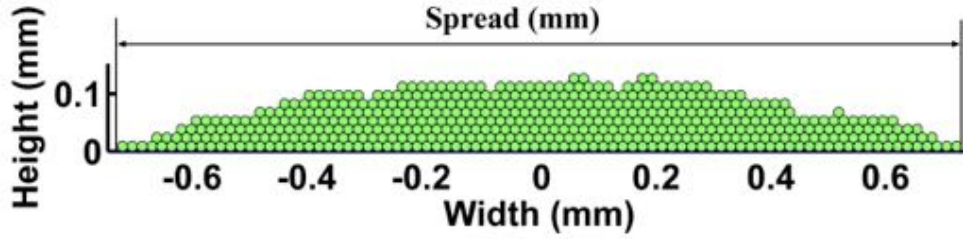
Figure 4.14: A sample simulation carried out for a system of 500 particles with $h = 5$ mm and $\beta = 3°$.

4.2.6 Results of simplified model

In order to demonstrate the behavior of the simplified model, the center to clamp distance, z_c, is kept constant while the height, h, is increased. The results are shown in fig. 4.15. As expected, the tow spread increases with h since increasing h will increase the normal component force, F_n, pushing the filaments into the surface with higher force. This means that the load equilibrium requires the tow to spread further as h increases.
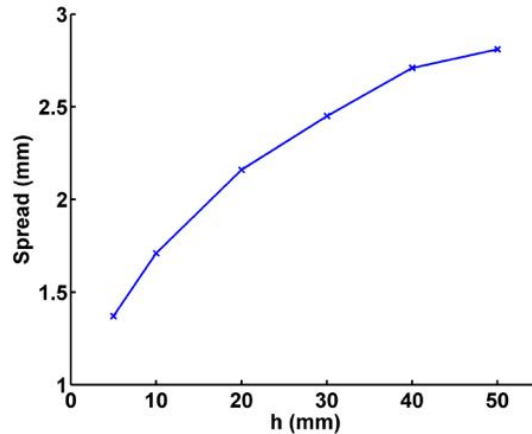

Figure 4.15: Spread of the tow as a function of height h, center to clamp distance $z_c = 96.2$ mm.

4.2.7 Number of Particles

The actual tow specimen has 3000 filaments, whereas for computational convenience only 500 particles were used to model the spreading behavior and the particles size was scaled to represent the actual system. One may argue that the spreading behavior of 500 particles does not represent the tow which has 3000 filaments. In order to investigate the effect of the number of particles, a system with 1000 particles was simulated using the simplified model. The results of the two systems with different number of particles was similar as shown in fig. 4.16. This means that as long as the number of particles are enough to offer an acceptable resolution, they will yield similar results. However, there surely is a critical number of particles, from which below that number the system is not represented correctly, especially when h increases.
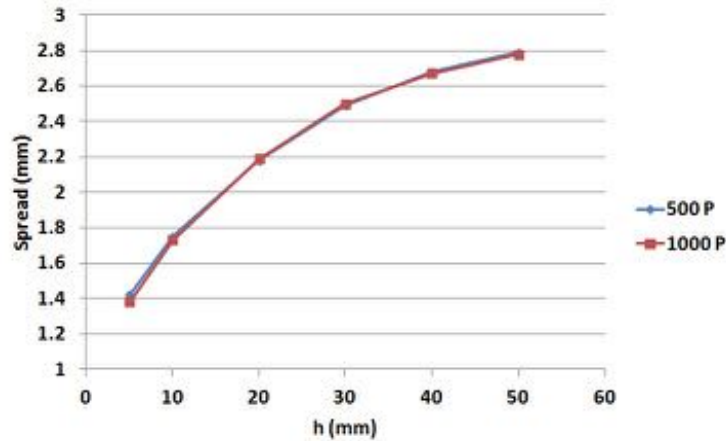
Figure 4.16: Spread of the particles as a function of height h for two systems with 500 and 1000 particles, $z_c = 96.2$ mm,.

In the next section, some of the simple assumptions will be replaced with more realistic models and the results will be compared to the simplified model.

4.3   Model Improvement

In the previous section, several assumptions were made to simplify the tow deformation model. In this section other features will be added:

1. Strain dependence of tension

2. Boundary particles and twist of filaments

3. Particle Radius Polydispersity

4. Cohesion of particles

5. Surface friction

After each model improvement is presented, the results of that model will be compared with that of the simple model.

4.3.1   Strain dependence of tension

Previously, it was assumed that tension is constant throughout all filaments. However, the tension depends on the elongation of the filaments and not all filaments have the same tension. This effect is increased when fibers with higher modulus are used, since a small difference in strain results in a significant difference in stress. The most obvious difference in length or strain arises from the fiber stacking. From fig. 4.10, it is clear that fibers with larger x and y-components are strained more than fibers close to surface of the spreader bar.

37

To calculate the length of the filaments, the length of the section which is not in contact with the bar, $2d_i$, should be added with the length of the filament wrapped around the bar, hence $L_i = 2(d_i + \beta R')$. R' is the radius of the bar plus the stacking effect of the tow. The initial unstrained length is defined as $L_0 = 2(d + \beta R)$ and the elasticity modulus of the material, E, is provided by the material supplier. In the simulations the actual modulus of the material was used, E= 230 GPa, and the unstrained length, L_0, was chosen as the length of the tow between the two clamps. Alternatively an offset value, L_e can be added to the initial and strained length to represent the extra hanging tow from both sides. The effect of this term is reducing the stiffness of the filaments. From this the tension in the filaments can be easily obtained from:

$$T_i = \frac{L_i - L_0}{L_0 + L_e} E A_i \tag{4.15}$$

where $A_i = 2\pi a_i^2$ is the cross section of each filament, calculated from its radius. The total tension of the tow is $T_t = \sum_{i=1}^{n} T_i$. Since it is desirable to have a determined tension in the tow the strain of the tow should be adjusted to obtain the total tension, $\tilde{T}$. if T_t is smaller than $\tilde{T}$, all of the filaments are strained further to reach the determined strain. The extra displacement required to reach $\tilde{T}$ is:

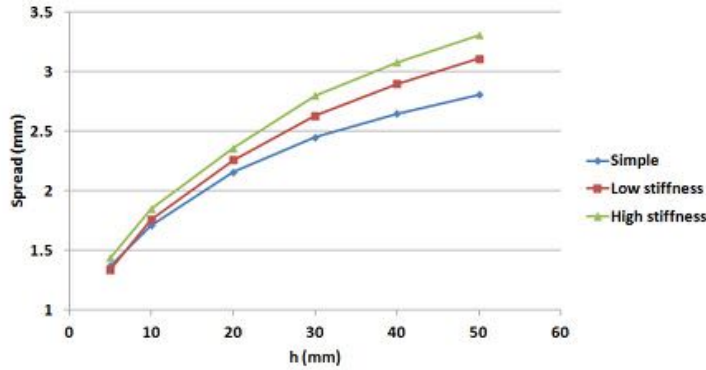$$\Delta L = \frac{\tilde{T} - T_t}{nEA/(L_0 + L_e)} \tag{4.16}$$

Figure 4.17: Spread of the tow as a function of height h, for the simple model and the strain dependent model for two different stiffness, $z_c = 96.2$ mm.

However, if T_t is larger than $\tilde{T}$, the extra strain should be taken off the filaments. This is not as straight forward as before since the least tensioned filaments already have a very small strain or tension and may obtain negative strain. Since filaments cannot endure compression the tension of those filaments should be set to zero as long as they have negative strain.

The results of the strain dependent model is presented in fig. 4.17 and compared to the simple model. For the high stiffness model L_e=0 mm and for the low stiffness model L_e=300 mm, which corresponds to the extra hanging length of the tow from the side bars in the experiments. At small heights h, the result of both models are similar. This is due to the fact that at small h the contact angle is small and therefore the gradient of
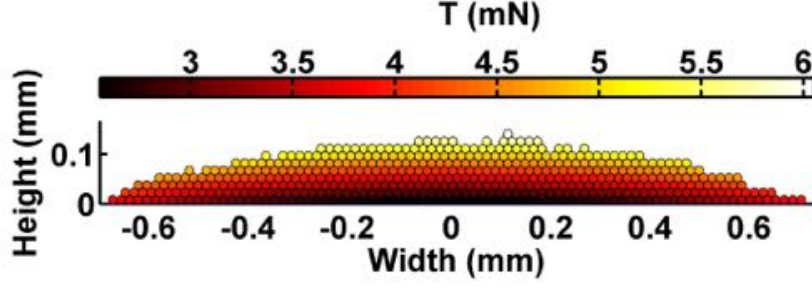
38

Figure 4.18: Spread of a strain dependent model displaying the tension difference between the filaments.

tension is less. As h increases the tension gradient increases. Therefore, filaments stacked at the top have a larger normal force component and cause the tow to spread further. The tension gradient is shown in fig. 4.18. The tension gradient is larger in the y-direction compared to the x- direction, this is due to the fact that displacement in the y-direction results in a larger strain or elongation.

The tension in each filament can also be used to determine filament failure. Since the tensile strength of the material, σ_T is known, the maximum tension filament i can carry can be easily obtained using $T_i^{\max} = \sigma_T A_i$. In this study this aspect will not be investigated in detail, but the tension did not exceed the maximum tensile strength of the filaments and was much smaller than that value in the worst case scenarios.

4.3.2 Boundary conditions

The boundary condition at the end of the can tow play a role on the lateral force. The initial assumption was that the filaments converge to a single point, while in reality, they have a specific shape at the boundary. In this case the force component calculation and fiber length calculation will differ. It will be assumed that the tow has a circular form at the clamps similar to the initial condition (fig. 4.12). Each filament is associated with a clamped filament at the boundary. The starting formation of the simulation is the same as the formation of the filaments at the clamps. This will change the lateral and normal force components to the following:

$$F_l = -2T\frac{x_i' - x_i^{clamp}}{d_i} \tag{4.17}$$

$$F_n = -2T\frac{h_i - h_i^{clamp}}{d_i} \tag{4.18}$$

where x_i^{clamp} and h_i^{clamp} are the $x-$ and $y-$components of the filament position at the clamp, respectively. The free contact tow length will become,

$$d_i = \sqrt{(x_i - x_i^{clamp})^2 + (y_i - h_i^{clamp})^2 + z_i^2} \tag{4.19}$$

Similar to the simplified model, simulations have been carried out with a constant z_c and varying the height h. The results of the simulation for the actual boundary model is
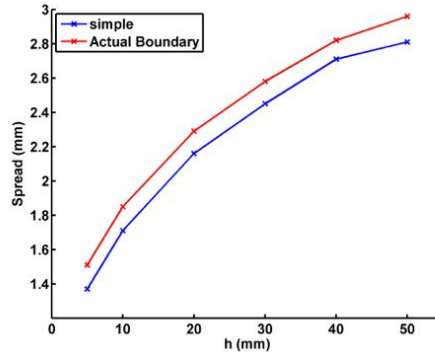
39

Figure 4.19: Comparison of the spread width of simple model with the actual boundary model, $z_c = 96.2$ mm.

presented in fig. 4.19. The trend is completely similar to the simple model except for an offset. This is due to the effect of a reduced lateral constraint on the filaments, allowing them to further spread.

4.3.3 Twist

This model is similar to the previous model, only that the initial formation of the filaments are different to those at the boundary. For this purpose, the filaments have been randomized at both of the clamps. When the simulation begins, the corresponding filament of the simulation will be another filament at the clamp. Altogether, there are three filament formations, one is used as an initial condition for the simulation and two are used to represent the side bar filaments. An example of randomized filaments is shown in fig. 4.20. The three colored particles correspond to each other. The rest of the filaments are also randomized, which is not displayed in the image. The same equations, eq. (4.18) and eq. (4.17), hold for this condition. The effect of the randomization can be seen in x_i^{clamp} and h_i^{clamp}. It can be said that the filaments are no longer parallel in the initial condition and that they have some twist.
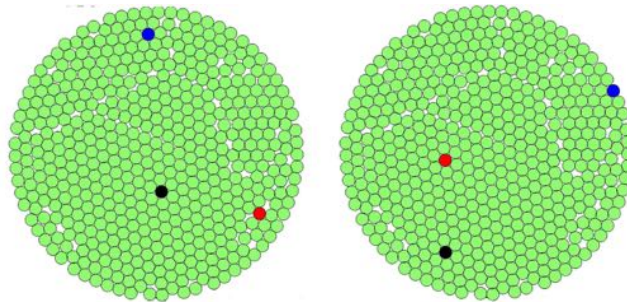

Figure 4.20: Three filaments have been colored to show how they correspond to each other.

The results of the simulation for the twist model is presented in fig. 4.21. The randomization at the clamps has reduced the spread to the simple model. As noted before,
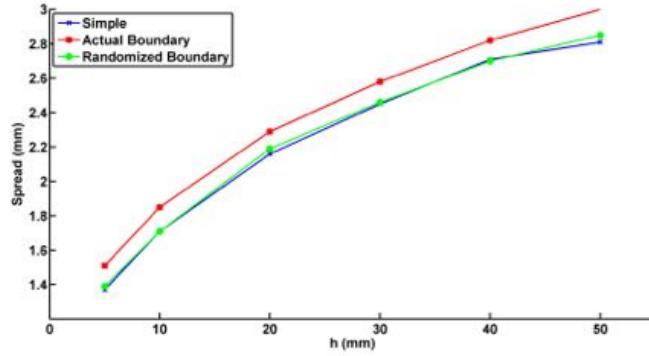
Figure 4.21: Comparison of the spread width of the randomized particle model with the simple and actual boundary model, $z_c = 96.2$ mm.

the actual boundary condition caused an offset to the spread, while the randomization has nullified the offset of the actual boundary model mimicking twist.

Another approach for twist is to apply a rotation to the clamp filaments at both sides. This can represent twist in the tow specimen. To apply a twist of φ, the original formation is twisted $-\varphi$ for one side clamp and $+\varphi$ for the other.
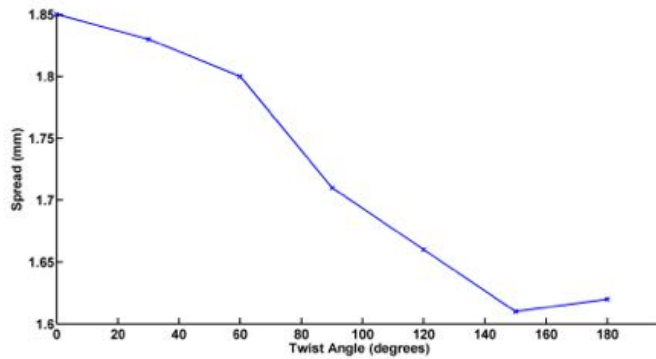

Figure 4.22: Spread of the tow as a function of the twist angle at the clamps, $z_c = 96.2$ mm, and height h=10 mm.

The simulations were carried out for one geometrical setup while the twist was applied. The twist varied from φ=0 degree, without twist, to φ=180 degrees. The results are plotted in fig. 4.22. It can be seen from the plot that the spread decreases as the twist is increased, as expected. The effect of twist is more significant from φ=60 degrees to φ=150 degrees. When the tow is twisted further after φ=150 degrees, the spread increases to some extent.

4.3.4 Polydispersity

In reality the filament radii are not monodisperse, but they have a radius distribution. Such a system can be modeled with bi or polydisperse particles. Since the filament radius distribution has already been obtained (section 3.1), those values will be used to study

41

the effect of polydispersity. In the simulations less particles are used with larger radii, therefore, the standard deviation is scaled accordingly, $stdev(const.a) = |const|.stdev(a)$. To model the polydispersity, a normal distribution of particles has been created using the measured average and standard deviation. The polydispersity is characterized using the moments of the particle size distribution [45–47]. For a polydisperse system, distributed according to a probability function $f(a)$ the k-th moment is defined as $\langle a^k \rangle = \int a^k f(a) da$ and the dimensionless moments are:

$$A = \frac{\langle a \rangle^2}{\langle a^2 \rangle} \quad O_1 = \frac{\langle a \rangle \langle a^2 \rangle}{\langle a^3 \rangle} \quad O_2 = \frac{\langle a^2 \rangle^3}{\langle a^3 \rangle^2} \tag{4.20}$$

A is know as the dimensionless width correction.

One may argue about the type of distribution of the particle size and that it may influence the outcome. In order to investigate the effect of the type of distribution, a bidisperse system with similar dimensionless moments are implemented. Ogarko and Luding [45] presented a formulation to obtain an equivalent bidisperse system. A bidisperse system, with radii a_1 and a_2, with N_1 and N_2 the number of particles of each kind, and $N = N_1 + N_2$. Thus the mixture can be classified by two parameters, the composition $n_1 = N_1/N$ and the size ratio $R_s = a_1/a_2$. The radius ratio and composition of the equivalent bidisperse system is R_s=0.973 and n_1=0.5. The k-th moment is defined as $\langle a^k \rangle = n_1 a_1^k + n_2 a_2^k$.

Table 4.2: Summary of simulated particle distributions

Particle size	$\langle a \rangle$ (μm)	$\langle a^2 \rangle$ (μm^2)	$\langle a^3 \rangle$ (μm^3)	A	O_1	O_2
Monodisperse	8.57	73.5	630.13	1	1	1
Polydisperse	8.57	73.459	629.775	0.9998	0.9996	0.9994
Equivalent Bidisperse	8.57	73.514	630.48	0.9998	0.9996	0.9994
Bidisperse 2	8.57	73.704	635.37	0.9972	0.9945	0.9918

In addition to the original filament distribution, a bidisperse system with a higher ratio $R_s = 0.9$ and composition N=0.5 was also simulated. The moments of the systems are presented in table 4.2. The results of the simulations are shown in fig. 4.23. The first observation is that the monodisperse system has the lowest spread. The polydisperse and its equivalent bidisperse system have similar results and their plots overlap (explaining why the polydisperse plot is not very visible), proving that the spread is independent of the type of distribution and only depends on the moments of the distribution. These two systems also had the ordered crystalline form similar to the monodisperse system. However, the bidisperse system with a larger radius ratio yields a significantly larger spread. It was also observed that the structure had lost its crystalline form at this radius ratio distribution.

4.3.5 Cohesion of particles

The filaments may display some cohesion behavior, this is especially true regarding the sized tow specimens. Cohesion will prevent spread of the filaments, as it tries to hold the
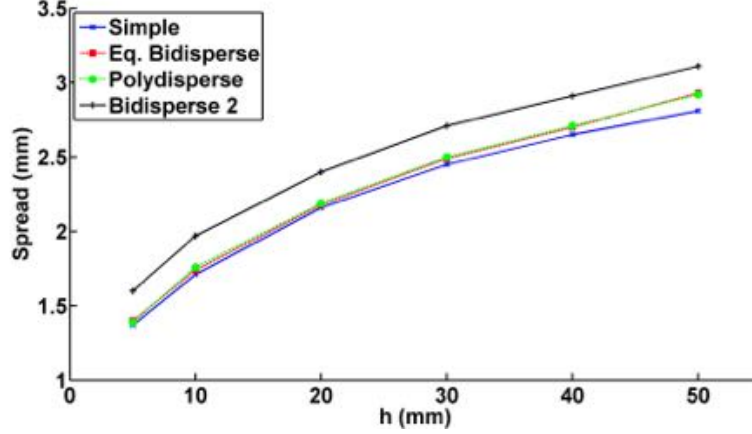
Figure 4.23: Spread of the tow as a function of the height h, $z_c = 96.2$ mm. The polydisperse model is plotted along with its equivalent bidisperse model. The simple model is presented for comparison. The 'bidisperse 2' system has a radius ratio of $R_s = 0.9$

tow together. This can be represented by adding a cohesion term to the force exerted on a particle:

$$\overrightarrow{F}_i = \overrightarrow{F}_i^{\,b} + \overrightarrow{F}_{ij}^{\,\mathrm{c}} - \overrightarrow{F}_{ij}^{\,\mathrm{cohesion}}. \tag{4.21}$$

The cohesion force is defined as $\overrightarrow{F}_{ij}^{\,cohesion} = (F_a s)\overrightarrow{n}$, where F_a is the average force per contact of some particles at the bottom center of the setup and s is cohesion factor. In order to obtain F_a, the average force per contact of the particles in the center are considered. All contacts within distance of three particles from the core of the particle packing are considered for F_a. The cohesion force is only activated when the particles come in contact, otherwise it is zero. Cohesion is zero at the beginning, since F_a has not been calculated yet. F_a is calculated once every thousand time steps. This value is used for the subsequent time steps until the next update of F_a. This means that the cohesion varies slightly throughout the simulation. It is also possible to define the cohesion relative to a constant property, such as the tow tension, however, this is not done here.

The simulations were carried out for one geometrical setup while the cohesion factor was changed. The cohesion factor was varied from $s=0$, without cohesion, to $s=5$, 5 times the average contact force. The results are plotted in fig. 4.24. It can be seen from the plot that the spread decreases linearly as the cohesion factor is increased. Ultimately at very high cohesion, the tow will not spread taking the form of a circular unspread tow. The cohesion model will only be applied when the sizing effect is required and it will be needed to find the suitable cohesion factor.

4.3.6 Surface friction

The spreading behavior of the tow may be influenced by friction. In this section a simple friction model is added to the system where friction is only applied between the particles and the surface. When a particle comes into contact with the surface, a normal reaction force F_r is applied from the surface to the particle. A constant coefficient of friction, μ, is
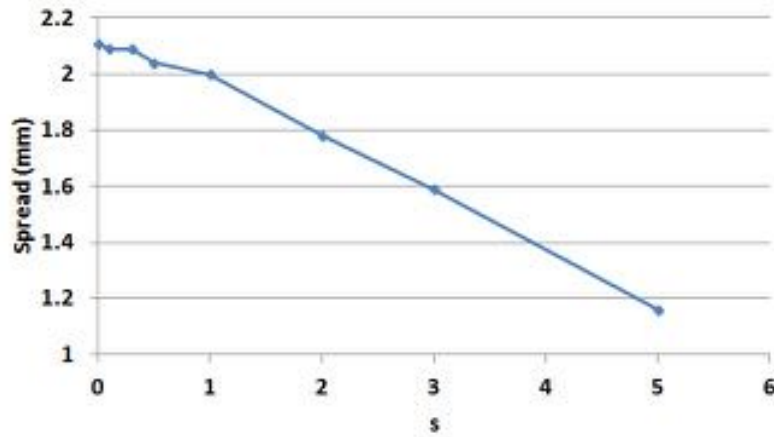
Figure 4.24: Spread of the tow as a function of the cohesion factor s (eq. (4.21)), $z_c = 96.2$ mm, and height $h=20$ mm.

used to calculate friction, regardless of kinetic or static friction. Friction can either bring a moving particle to a stop or reduce its velocity, or prevent it from moving, based on the velocity and lateral force on the particle.

A friction coefficient of $\mu=0.1$ was used. First, the virtual damping coefficient and height were set to $b=0.5$ kg/s and $h=3$ mm to bring the particles to rest on the surface. Then b was set to zero to minimize the virtual damping effect and h was increased for the purpose of simulation. The result of the friction model is shown in fig. 4.25 and compared to the simple model. It can be seen that applying the surface friction reduces the spreading behavior up to $h=30$ mm and prevents further spread when h is increased.
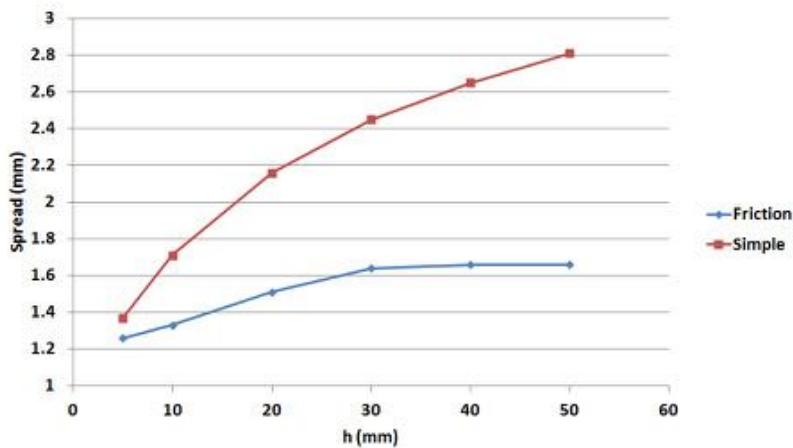

Figure 4.25: The spread of the tow as a function of height h for the simple and friction model.

The simple friction model cannot correctly model the friction. It could be that if a more comprehensive friction model, which allows rotation and rolling of the particles, is used, better results would be achieved. However, a more complicated friction model will not be discussed in this study.

44

4.3.7 Model feature summary

In the previous sections the DEM method was introduced and implemented. After identifying the relevant forces, they were translated to the model. First, a simplified model was presented and in the next steps other features were added to the model and their effects were observed and discussed briefly. Not all of the features will be used in the final model. The experimental results (section 3.3) should be used to determine which features are relevant and which are not. For instance it was determined that twist will be prevented as much as possible. Upon visual inspection of the tow it was determined that the twist was less than 0.6 twists per meter, hence this will be applied to the final model to account for existing twist, which also requires applying the actual boundary model. According to fig. 4.22, this amount of twist will influence the spread less than 1 percent. An important outcome of the experiments was that the spread was strain dependent, therefore strain dependency will be applied to the final model, both low and high stiffness system properties will be used and compared. As for polydispersity, the actual polydispersity of the tow will be used, although it was observed that the effect of polydispersity is minimal at such a narrow distribution. On the other hand cohesion will be used but only for experimental results regarding sized tow specimens. The cohesion factor will be chosen in a way to represent the sizing effect and fit with the experimental results. It was determined that a cohesion factor of $s=4$ (section 4.3.5) gives satisfactory results. Surface friction is not applied to the model, since it does not give correct results. This may be due to the fact that the simple friction model is inefficient, and the particles should be allowed to roll on the surface as well as slide.

In the results section this final model is used and simulations which correspond with actual experiments are carried out. The geometrical variations presented in section 3.2.2 will be used. Since the model is only intended to predict the spreading behavior of one cross section, a spreader bar radius of $R=3$ mm will be used to minimize the contact surface. The simulations are carried out using the parameters in table 4.3. The amount of twist, twist per meter, is equal for both $z_c=35$ mm and $z_c=96.2$ mm but since the length of the tow is different for these two conditions the amount of twist at the clamps differ.

Table 4.3: Summary of the parameter variation

Variation	$z_c(mm)$	h (mm)	clamp twist	Remarks
Geometry	35	5,10,20,30	7.6°	
	96.2	5,10,20,30	20°	
Cohesion	96.2	5,10,20,30	20°	Cohesion factor $s=4$

4.4 Continuum fields

Granular materials are discrete elements. A bucket filled with stone can be considered a granular medium. If a random point is chosen, there may or may not be material in that point. If there is no material, the mass, stress, strain is zero at that point. In order to observe stress in granular materials, experiments can be carried out using photo-elastic

materials to characterize the stress on the disks using photoelasticity [48]. Therefore, stress in a granular material is not distributed uniformly but is conducted along so-called force chains which are networks of grains resting on one another. Looking at the discrete grain, one can define microscopic properties which are local properties which vary greatly from one point to the next.

This is also true for any other solid, liquid or gaseous material, since all materials are consisted of discrete elements, molecules and atoms. If done correctly, any material can be modeled using discrete elements. For continuous materials this can be done using molecular dynamics. On the other hand, macroscopic properties are properties which do not exhibit very large gradients in neighboring points and are continuous, such as volume fraction, mass density, stress, strain, etc. Efforts to connect molecular dynamics with macroscopic quantities dates back to studies carried out by Boltzmann. The Kinetic theory of gases explains macroscopic properties of gases, such as pressure, temperature, or volume, by considering their molecular composition and motion.

Macroscopic continuum equations for the description of the behavior of granular media rely on constitutive equations for stress, strain, and other physical quantities describing the state of the system. One possible way of obtaining an observable like the stress is to perform discrete particle simulations and to average over the microscopic quantities in the simulation, in order to obtain an averaged macroscopic quantity. In order to obtain macroscopic properties two methods are available, the cell averaging method and the coarse graining method. These methods and their formulations are explained extensively in [36, 49]. A short summary of the continuum fields using the cell averaging method is presented below. The particle area is binned using the Voronoi tessellation, in which each particle is inside one cell. For further details refer to the articles.

In this model the particles are cylindrical with height $h_p = 2R \sin \beta$. The total contact force is applied on the cylinders, therefore, the contact force is first divided by the height h_p and the calculations are carried out for the 2-dimension plane using the force per unit length $f_{ij}^c = F_{ij}^c / h_p$. This will also correct the units for calculation of pressure and stress.

The first continuum field is the volume fraction, which is defined as the ratio of the area of the particle A_p, to the area of the Voronoi cell of that particle A_{tot}:

$$\nu = \frac{A_p}{A_{\text{tot}}} \tag{4.22}$$

The second quantity is the stress σ in the original coordinate system and from that, the stress components σ_{xx}, σ_{yy} and τ_{xy} are extracted. For the Voronoi approach, the stress tensor for cell i corresponding to particle i is obtained using:

$$\sigma_i = \frac{1}{A_{\text{tot}}} \Sigma f_{ij}^c \otimes l^{pc} \tag{4.23}$$

where the sum is over all contacts on particle i, l^{pc} is the branch vector going from the center of the particle to the contact point and $\otimes$ is the dyadic product.

The principal stresses are obtained from the following req:

$$\sigma_{1,2} = \frac{\sigma_{xx} + \sigma_{yy}}{2} \pm \sqrt{\left(\frac{\sigma_{xx} - \sigma_{yy}}{2}\right)^2 + \tau_{xy}^2} \tag{4.24}$$

46

The pressure is simply $P = (\sigma_1 + \sigma_2)/2$ and the deviatoric stresses are, $s_{xx} = \sigma_{xx} - P$ and $s_{yy} = \sigma_{yy} - P$. Knowledge of the stresses allows the determination of the orientation of the principal planes.

In the following the Voronoi method is applied to the simulation results of the final model, where z_c=96.2 mm and h=5 mm. Also note that there are less than 500 particles in the following Voronoi tessellation plots. This is due to the fact that the Voronoi tessellation is not bounded correctly for the outer particles, therefore they are not displayed. The lower particles in contact with the boundary were bounded by mirroring those particles relative to the boundary.

4.5   Continuum field results

The continuum fields were obtained for monodisperse and bidisperse system using the Voronoi cell method. Some of the fields are also presented using the coarse graining method for comparison. The continuum results and plots were verified by dividing the total normal force component of the tow by the contact surface and comparing this value to the σ_{yy}; it was confirmed that the plots are correct. The continuum quantities are obtained for the monodisperse and the equivalent bidisperse systems of table 4.2. The convention for the stress tensors is that negative is compressive stress and pressure is plotted as positive, i.e. $-P$ is presented.

The volume fraction of the particle packing is shown in fig. 4.26 and fig. 4.27 for the monodisperse and bidisperse systems, respectively. For the monodisperse system, the volume fraction is nearly similar for all particles except for the particles in contact with the boundary, which is due to the fact that their cells have a higher A_{tot}. The volume fraction of the bidisperse system seems somewhat different. Neglecting the boundary particles and considering the scale of the color bar apparently the variation is not very large, but even though the structure can still be considered ordered. The few cells on the top which do not have a regular hexagonal form are due to the Voronoi tessellation procedure and are ignored. The coarse grained volume fraction is shown in fig. 4.28. It can be seen that the local variations are smeared out compared to the Voronoi method and that it is an ordered packing. It should also be noted that the volume fraction $\nu \cong 0.91$ is the close packed hexagonal ratio for circles in 2-dimensions.

The stress component σ_{xx} is shown in fig. 4.29 and fig. 4.30 for the monodisperse and bidisperse systems, respectively. The stress gradually increases from a minimum, from the sides, to a maximum to the core of the particle packing, note that also here the boundary particles at the bottom display less stress due to larger A_{tot}. This stress trend is also observed for the bidisperse system, however, the polydispersity has introduced inhomogeneity in stress distribution, resulting in some particles with much larger stress and some with less stress. There seems to be a sequence of connected particles which have a high stress. The stress σ_{xx} is also plotted for the bidisperse system using the coarse graining method in fig. 4.31 (note the convention of stress is reversed). This method gives similar results compared to the Voronoi method, only with smoother gradients.

The stress component σ_{yy} is shown in fig. 4.32 and fig. 4.33 for the monodisperse and bidisperse systems, respectively. The general trend here is that σ_{yy} increases from the top to the bottom and is higher where more particles are stacked above each other. The

polydispersity also introduces a lot of inhomogeneity in σ_{yy}, similar to σ_{xx} plot.

The pressure plot for the monodisperse and bidisperse systems is presented in fig. 4.34 and fig. 4.35, respectively. The pressure is minimum at the boundary and increases to the maximum at the core. Again, the polydispersity has caused some particles to be under more pressure compared to their neighbors. The shear stress τ_{xy} is shown for the monodisperse and bidisperse systems in fig. 4.36 and fig. 4.37, respectively. There is very little shear stress for the monodisperse system compared to the bidisperse system. The shear stress shows the tendency of the particles to roll or slip over each other. This may explain the extra spread width w for bidisperse systems due to high shearing stresses.

The deviatoric stresses s_{xx} and s_{yy} are shown in fig. 4.38, fig. 4.40, fig. 4.39 and fig. 4.41 for the mono and bidisperse systems. Other than the usual inhomogeneity for the bidisperse system and the general trend of a maximum stress at the core, the interesting point is that s_{xx} is generally positive and s_{yy} is negative. This shows the higher contribution to pressure from σ_{yy}.

Next, the principal stresses, σ_1 and σ_2, are plotted in their orientation for all particles at the particle center, in fig. 4.42 and fig. 4.43 for the mono- and bidisperse systems, respectively. From fig. 4.42, it can be seen that the principal stress are in the original coordinate for the monodisperse system. However, the principal stress plot and orientations of the bidisperse system shows that not only the stress and pressure magnitude is different but the principal directions also vary significantly. The principal stresses have been normalized using the particle pressure and shown in fig. 4.44 and fig. 4.45 for the two systems. The particles with small principal stresses at the boundary are better visible here.

One important conclusion is that such a small and narrow polydispersity with an ordered structure causes such large variations in pressure and stress distributions. Such large variations can cause premature failure of filaments and components. Many types of tow materials fail under compressive pressure. Another important conclusion is that DEM provides the possibility of taking into account such inhomogeneous distributions which is not possible in continuum mechanics. When continuum methods are used to obtain fields such as tow stress and pressure, these variations and realistic issues cannot be identified. DEM takes the random and developing structure into account. A small dispersity in the particle size greatly affected the pressure and orientation of principal stresses in the structure and caused large stress inhomogeneity. The amount of stress inhomogeneity would increase as the size difference increases or the stiffness of the particles increase. This is due to the fact that as the size difference and stiffness are reduced the particles can overlap and distribute the pressure on more particles. Defining a parameter such as $(a_2 - a_1).(k)$ can provide insight on the effect of particle size and stiffness.
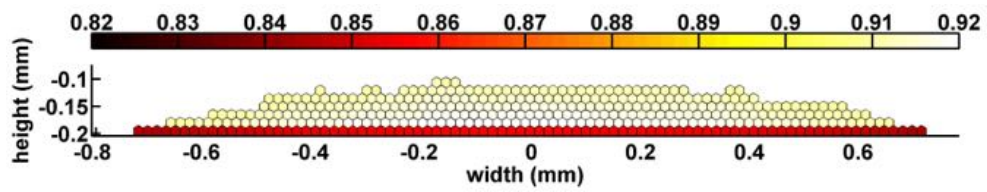
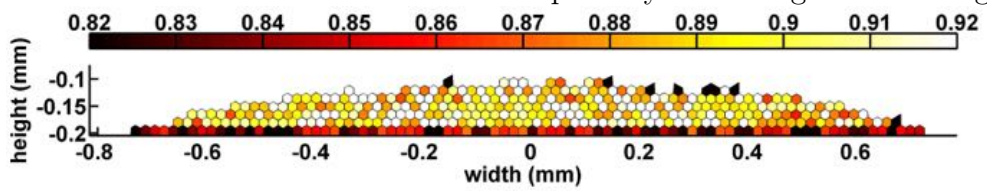Figure 4.26: Volume fraction of the monodisperse system using Voronoi diagram.

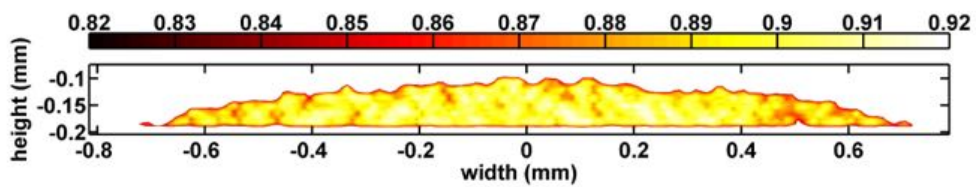Figure 4.27: Volume fraction of the bidisperse system using Voronoi diagram.

Figure 4.28: Volume fraction of the bidisperse system using coarse graining.
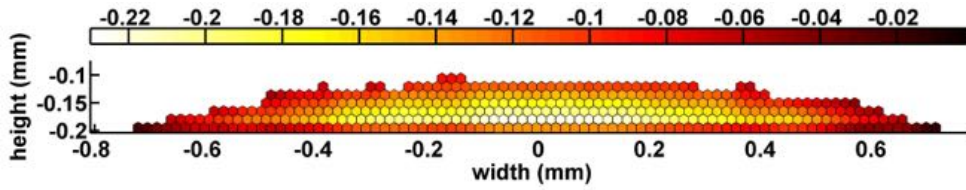
Figure 4.29: σ_{xx} plot of the monodisperse system using Voronoi diagram. The units are in MPa.
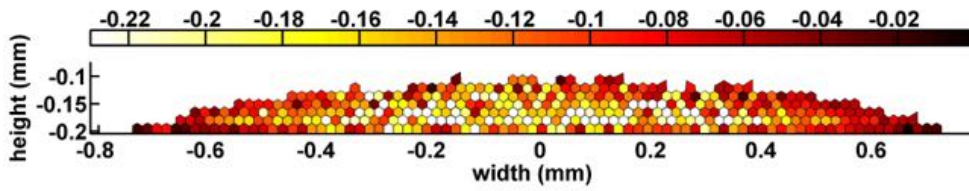

Figure 4.30: σ_{xx} plot of the bidisperse system using Voronoi diagram. The units are in MPa.
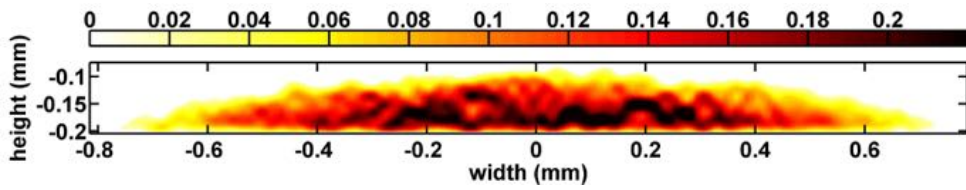

Figure 4.31: σ_{xx} plot of the bidisperse system using the coarse grained system. The units are in MPa and the convention is that positive stress is compressive.
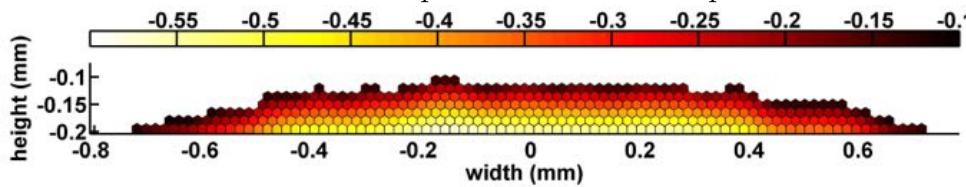

Figure 4.32: σ_{yy} plot of the mono system using Voronoi diagram. The units are in MPa.
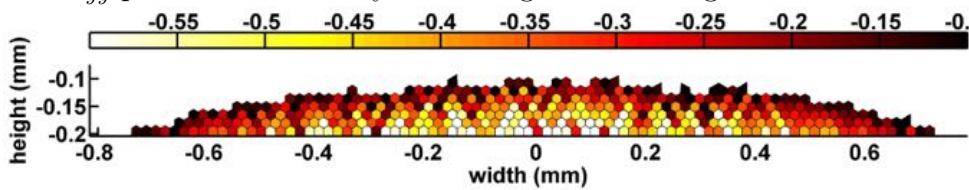

Figure 4.33: σ_{yy} plot of the bidisperse system using Voronoi diagram. The units are in MPa.
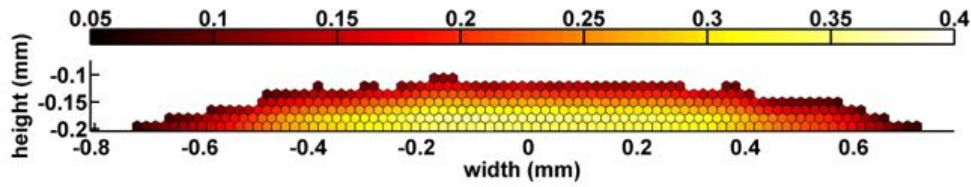
Figure 4.34: Pressure plot of the monodisperse system using Voronoi diagram. The units are in MPa.
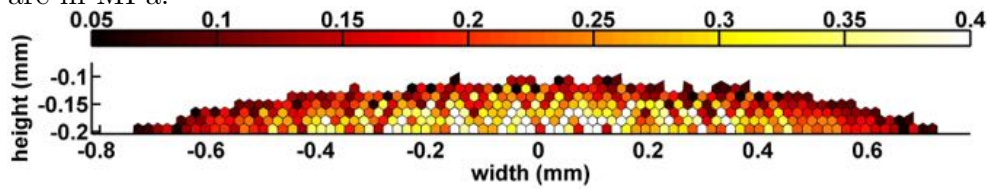

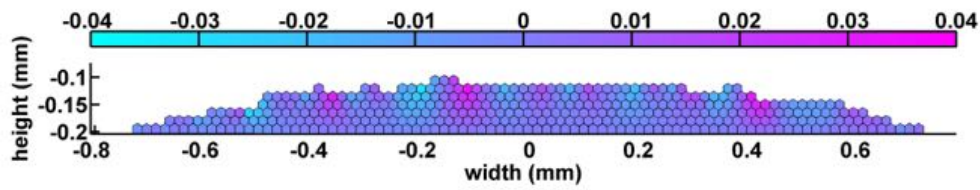Figure 4.35: Pressure plot of the bidisperse system using Voronoi diagram.

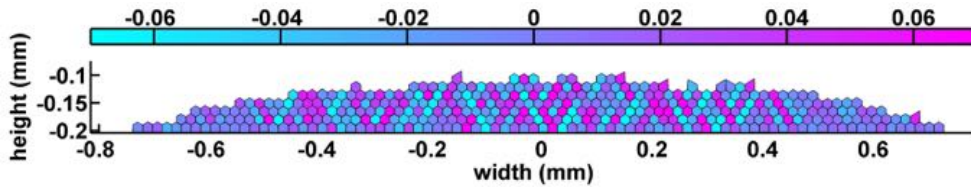Figure 4.36: σ_{xy} plot of the mono system using Voronoi diagram. The units are in MPa.

Figure 4.37: σ_{xy} plot of the bidisperse system using Voronoi diagram. The units are in MPa.

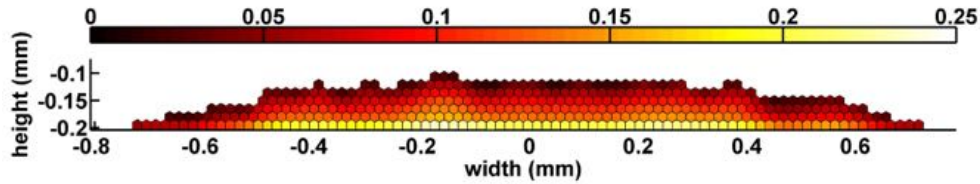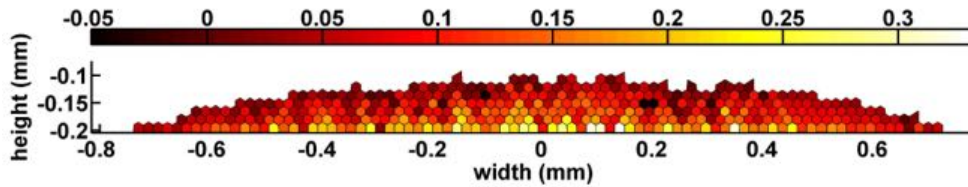Figure 4.38: deviatoric stress plot of monodisperse system s_{xx} using Voronoi diagram.

Figure 4.39: deviatoric stress plot of bidisperse system s_{xx} using Voronoi diagram. The units are in MPa.
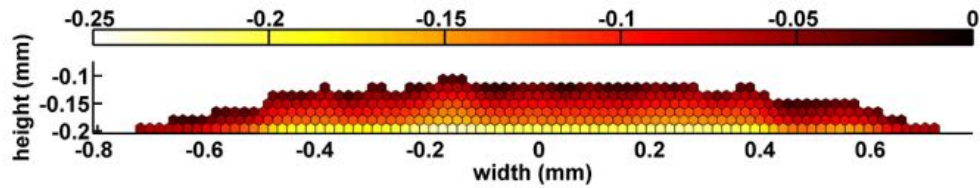

Figure 4.40: deviatoric stress plot of monodisperse system s_{yy} using Voronoi diagram. The units are in MPa.
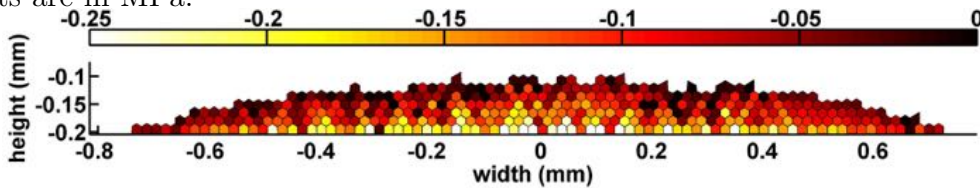
Figure 4.41: deviatoric stress plot of bidisperse system s_{yy} using Voronoi diagram. The units are in MPa.
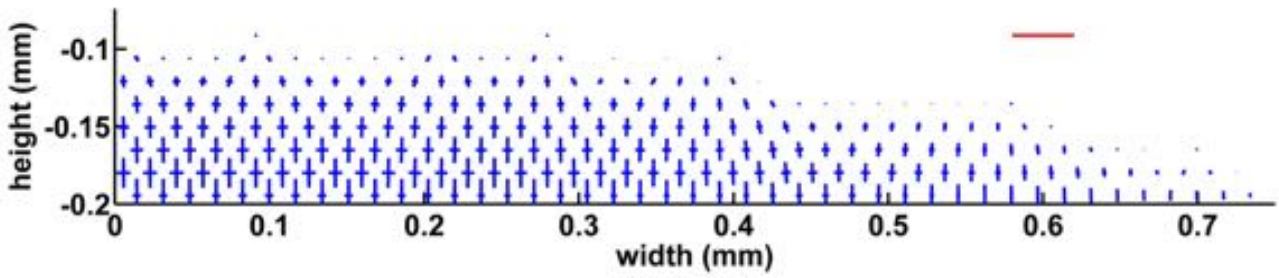
Figure 4.42: The principal stresses plotted at the particle location with their direction for the monodisperse system. The red scale line represents 1 MPa.
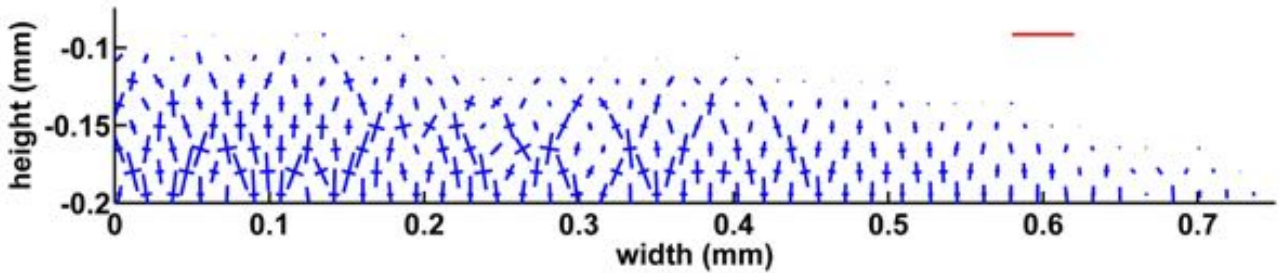
Figure 4.43: The principal stresses plotted at the particle location with their direction for the bidisperse system. The red scale line represents 1 MPa.
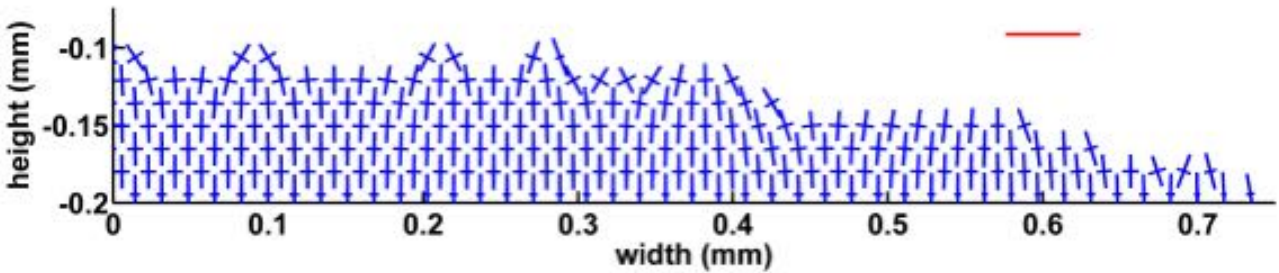
Figure 4.44: The normalized principal stresses plotted at the particle location with their direction for the monodisperse system. The stresses have been normalized with the pressure at those points. The red scale line represents 3 Mpa/Mpa.

Figure 4.45: The normalized principal stresses plotted at the particle location with their direction for the bidisperse system. The stresses have been normalized with the pressure at those points. The red scale line represents 3 Mpa/Mpa.

4.6 Results

The results for the geometrical variations and application of cohesion are shown in fig. 4.46. For each geometry two systems with high and low stiffness are s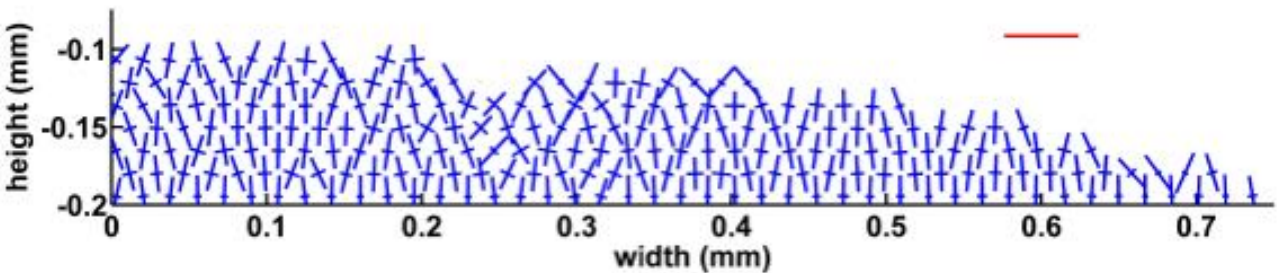imulated (for the high stiffness and low stiffness systems refer to section 4.3.1). These results will be used for comparison with the experiments.
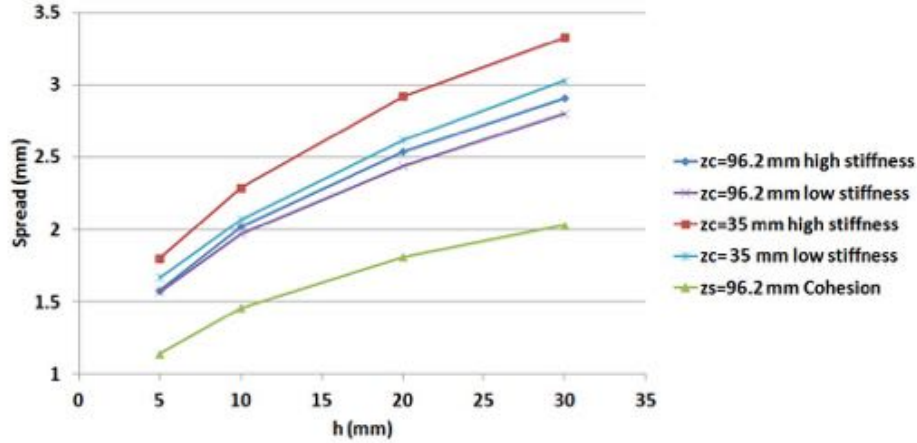
Figure 4.46: Spread as a function of height h for different geometries and with cohesion. For different geometries high and low stiffness parameters were used (section 4.3.1) and for the cohesion model only high stiffness

4.6.1 Geometrical variation

The simulation was conducted for z_c=35 mm and z_c=96.2 mm. As discussed in section 4.3.1, the strain dependence of tension will cause a higher spread, compared to constant tension throughout all filaments. However, it is observed from fig. 4.46 that the spread also increases as z_c is reduced. This is due to the fact that as z_c is reduced, the strain gradient increases between the particles and particles which have a higher height h_i carry more of the tension. As they move down, causing the structure to spread, their tensions reduce.

4.6.2 Cohesion

In order to be able to correctly model the sizing effect, first the correct cohesion factor has to be obtained. An iteration for different cohesion factors for the simple model was presented in section 4.3.5. A suitable fit with the experimental results was obtained when a cohesion factor of s=4 was used. As expected the cohesion reduces the final spread (fig. 4.46).

4.7   Summary

In this chapter, the DEM method was thoroughly introduced and the relevant parameters were explained. A simple model for the spreading behavior was presented. Several features were added to the simple model and the results and influence of each feature was discussed, then it was determined which features will be kept for the final model.

The extraction of continuum quantities from discrete assemblies was briefly introduced and several continuous quantities were calculated for the final model, and the obtained continuum fields were discussed. A very important conclusion of this section was that when polydisperse particles are used, as is in reality, the stress and pressure distribution become inhomogeneous, contrary to continuum models.

Finally, the spread results were plotted for the final model for different geometrical and material parameters (sizing). In the next chapter, this model and its results will be used for comparison with the experimental results obtained in chapter 3.

Chapter 5

Discussion

The experimental approach and its results were presented in chapter 3 and the possible spreading mechanisms and important factors in spreading were discussed. Chapter 4 was dedicated to the Discrete Element Method (DEM). After introducing DEM, a simplified model was devised which represented the spreading experiments. Several features were added to the simplified model and a final model with all of the relevant features was implemented. In this chapter, first the experiment, model and literature (Wilson's prediction [27]) results will be presented together and compared in section 5.1. After drawing the final conclusions in section 5.2, some recommendations are given for future research on this subject in section 5.3.

5.1   Comparison of model, experiments and literature

The model, experiments and literature are compared for three different conditions. For the first two conditions, geometrical variations are taken into account and the results of the three different approaches are presented. The experiments for these variations were carried out for desized tow specimens and the error bars represent the standard deviation of the experiments. The simulations were carried out for low and high stiffness conditions (For more details on the two models refer to section 4.3.1).

The results for the clamp to center distance z_c=96.2 mm are presented in fig. 5.1. The low stiffness model is within 4 percent and the high stiffness model is within 7 percent of the measurements. Both models predict the tow spread to good accuracy, but they both exceed the experiments by a small amount. This could arise from the fact that the radius of the spreader bar in the experiments was not small enough. Wilson's model overshoots the experimental results by approximately 25 percent. As observed in fig. 3.12 (section 3.3.1), the spread increases when the spreader bar radius is reduced. It could be that if the size of the spreader bar is reduced, the experimental results would increase to obtain a better fit with the model. This could be attributed to the fact that since only one cross section is modeled, when the bar radius increases, the contact length of the tow and consequently the load distribution change and the model will not be valid. Another possibility is that if comprehensive friction is added to the model, the model results would decrease.

When the clamp to center distance is reduced to z_c=35 mm, the model results and

Wilson's prediction are all within 10 percent range of the measurements. Due to increase in tension gradient between the filaments, the spread increases both in the model and the experiments. If strain dependency is not included, the model would act similar to Wilson's prediction, and become independent of z_c. This is a very serious flaw in Wilson's model. It is also observed that the measurement results are between the high stiffness and low stiffness models. The difference between these two models was taking the free hanging length of the tow into account or neglecting the effect from the hanging length. This could mean that the actual stiffness is somewhere between these two models.

The results for the experiments with the sized material is shown in fig. 5.3 along with the high stiffness model with cohesion and Wilson's prediction. Since Wilson does not include material parameters it gives the same results as the two previous plots. For the model, a cohesion factor of $s=4$ was used to simulate the existence of sizing. Although the model results are within the range of the measurements, the slope is smaller for the model. At small h, the predicted spread is higher than the measurements, and at higher h the predicted spread is lower. The smaller slope of the model can be related to the definition of the cohesion. Since the cohesion force is related to the contact forces at the core of the packing, at higher h the contact force increases, resulting in a larger cohesion force calculation.

5.2 Conclusions

The first conclusion is that the DEM model was able to predict tow spreading accurately, since it gave correct results for two different geometrical setups, crossing out the possibility of a random correct fit. The cohesion factor had to be iterated in order to fit the sized material experiments, but yielded accurate results for different heights h. The DEM model is also suitable from the aspect that it can be further developed to include friction and other features.

Wilson's model did not take into account several parameters, including the significant effects of strain dependence of filament tension and sizing on tow spread. Although Wilson can give a quick indication of the approximate tow spread, it cannot give an accurate one. This is due to the fact that important parameters such as the material properties and tension difference between the filaments are not taken into account.

Figure 5.1: Model (high stiffness and low stiffness), experiment and literature results plotted as a function of height h, z_c=96.2 mm without sizing.
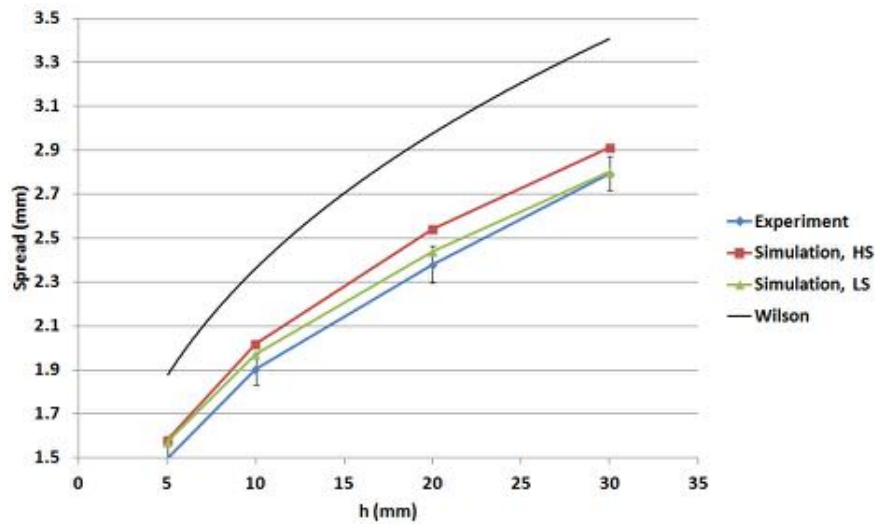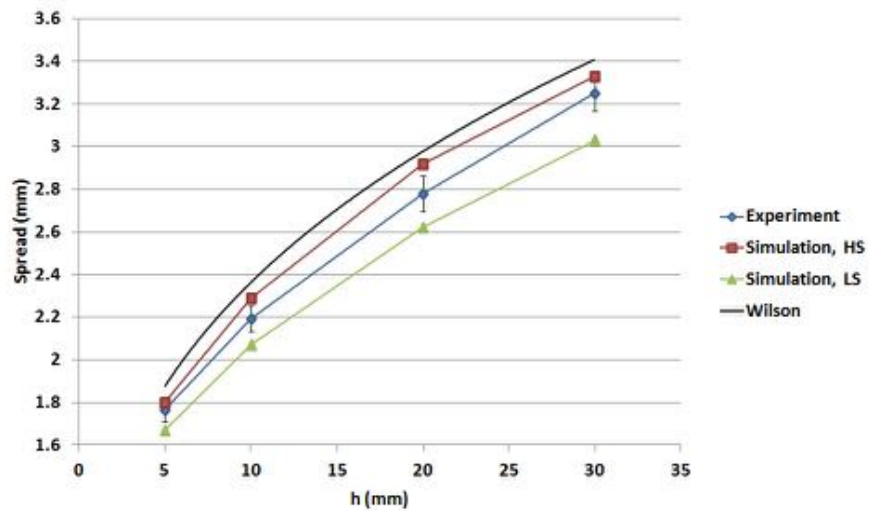

Figure 5.2: Model (high stiffness and low stiffness), experiment and literature results plotted as a function of height h, z_c=35 mm, without sizing.
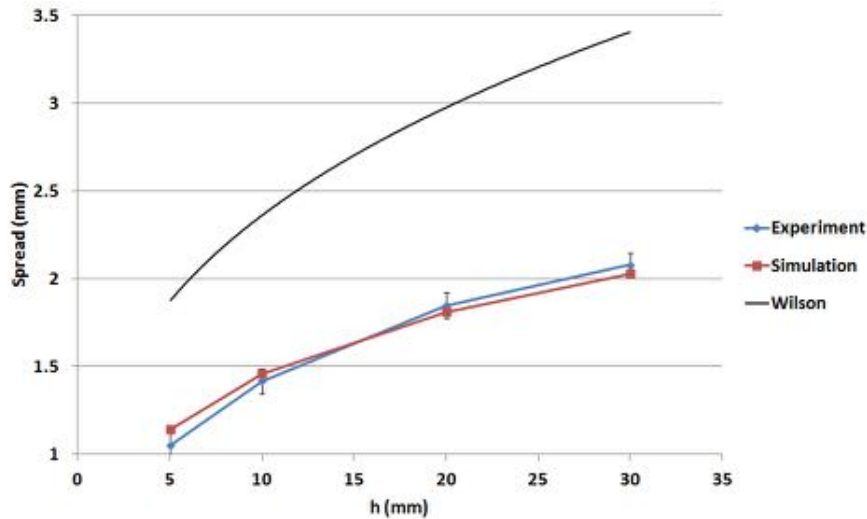
Figure 5.3: Model (high stiffness), experiment and literature results plotted as a function of height h for the system with sizing (experiments) or cohesion (model), $s=4$, $z_c=96.2$ mm.

5.3 Recommendations for future studies

A discrete element model was presented in this study to predict the spreading behavior of tows. The spreading behavior is one of several tow deformation mechanisms, such as bending and twisting. It was found that the model is able to predict the spreading behavior of a tow cross section well within 10 percent of the experiments. The added value of this model was that it was able to take into account important aspects of the experiments which greatly influence the spread of the tow.

Adding a comprehensive friction model is the next step to obtain a more realistic prediction of the tow spreading behavior. It should be determined if such a friction model would solve the issues of the simple friction model. Studying the surface effects of the spreader bar is another interesting possibility. Carrying out experiments with different types of metals, ceramics and plastics with different roughness could yield interesting results. It has been shown that when a very smooth spreader bar is used, adhesion also plays a role in the deformation and spread of the tow [50]. Surface adhesion can be easily implemented in the model. Also the effect of surface features such as roughness and other geometrical aspects can be included in the future.

It is expected that if the model is generalized and implemented in three dimensions it should be able to predict the deformation of tows. But preliminary to that, a more efficient contact algorithm should be implemented. When this is done, a single filament can be modeled with cylindrical elements which are attached together. A tow can be modeled with a few hundred of these chain elements. With an efficient algorithm, static problems can be carried out with very low computational expense. If this is done correctly, the model should be able to catch the effect of the spreader bar size. This model can be used to predict tow behavior in many production processes, such as braiding, weaving and filament winding. The chain elements can be given bending and torsional stiffness

to open up the possibility of modeling other deformation mechanisms. It could be useful in the better understanding of locking during shearing of fabric materials. It will also be possible to calculate the permeability of the structure and model resin impregnation in the tow using FEM.

By analyzing the stress components and pressure in the filaments and throughout the tow structure, it is possible to obtain other failure criteria, which are not available when the tow is modeled as a continuum. This opens up many possibilities in the analysis of various production processes, where tow and filament pressure have significant impact on the process.

Bibliography

[1] C. Williams, J. Summerscales, and S. Grove, "Resin infusion under flexible tooling (rift): a review," *Composites Part A: Applied Science and Manufacturing*, vol. 27, no. 7, pp. 517 – 524, 1996.

[2] Q. Govignon, S. Bickerton, J. Morris, and P. A. Kelly, "Full field monitoring of the resin flow and laminate properties during the resin infusion process," *Composites Part A: Applied Science and Manufacturing*, vol. 39, no. 9, pp. 1412 – 1426, 2008.

[3] M. K. Kang, W. I. Lee, and H. T. Hahn, "Analysis of vacuum bag resin transfer molding process," *Composites Part A: Applied Science and Manufacturing*, vol. 32, no. 11, pp. 1553 – 1560, 2001.

[4] D. H. Lee, W. I. Lee, and M. K. Kang, "Analysis and minimization of void formation during resin transfer molding process," *Composites Science and Technology*, vol. 66, no. 16, pp. 3281 – 3289, 2006.

[5] R. S. Feltman and M. H. Santare, "Evolution of fibre waviness during the forming of aligned fibre/thermoplastic composites," *Composites Manufacturing*, vol. 5, no. 4, pp. 203 – 215, 1994.

[6] D. C. Guell and T. D. Papathanasiou, *Flow-induced alignment in composite materials.* Cambridge: Woodhead, 1997.

[7] H. M. Hsiao and I. M. Daniel, "Effect of fiber waviness on stiffness and strength reduction of unidirectional composites under compressive loading," *Composites Science and Technology*, vol. 56, no. 5, pp. 581 – 593, 1996.

[8] H. M. Hsiao and I. M. Daniel, "Elastic properties of composites with fiber waviness," *Composites Part A: Applied Science and Manufacturing*, vol. 27, no. 10, pp. 931 – 941, 1996.

[9] G. Karami and M. Garnich, "Effective moduli and failure considerations for composites with periodic fiber waviness," *Composite Structures*, vol. 67, no. 4, pp. 461 – 475, 2005.

[10] B. D. Allison and J. L. Evans, "Effect of fiber waviness on the bending behavior of s- glass/epoxy composites," *Materials & Design*, vol. 36, no. 0, pp. 316 – 322, 2012.

[11] A. G. Prodromou and J. Chen, "On the relationship between shear angle and wrinkling of textile composite preforms," *Composites Part A: Applied Science and Manufacturing*, vol. 28, no. 5, pp. 491 – 503, 1997.

[12] P. Potluri, D. A. P. Ciurezu, and R. B. Ramgulam, "Measurement of meso-scale shear deformations for modelling textile composites," *Composites Part A: Applied Science and Manufacturing*, vol. 37, no. 2, pp. 303 – 314, 2006.

[13] J. Cao, R. Akkerman, P. Boisse, J. Chen, H. S. Cheng, E. F. de Graaf, J. L. Gorczyca, P. Harrison, G. Hivet, J. Launay, W. Lee, L. Liu, S. V. Lomov, A. Long, E. de Luycker, F. Morestin, J. Padvoiskis, X. Q. Peng, J. Sherwood, T. Stoilova, X. M. Tao, I. Verpoest, A. Willems, J. Wiggers, T. X. Yu, and B. Zhu, "Characterization of mechanical behavior of woven fabrics: Experimental methods and benchmark results," *Composites Part A: Applied Science and Manufacturing*, vol. 39, no. 6, pp. 1037 – 1053, 2008.

[14] H. W. Chandler, B. J. Devlin, and A. G. Gibson, "A model for the continuous impregnation of fibre tows in resin baths with pins," *Plastics, Rubber and Composites Processing and Applications*, vol. 18, no. 4, p. 215, 1992.

[15] R. J. Gaymans and E. Wevers, "Impregnation of a glass fibre roving with a polypropylene melt in a pin assisted process," *Composites Part A: Applied Science and Manufacturing*, vol. 29, no. 56, pp. 663 – 670, 1998.

[16] G. Xian, H. T. Pu, X. S. Yi, and Y. Pan, "Parametric optmisation of pin-assisted-melt impregnation of glass fiber/polypropylene by taguchi method," *Journal of Composite Materials*, vol. 40, no. 23, pp. 2087–2097, 2006.

[17] B. Cornelissen, L. Warnet, and R. Akkerman, "Friction measurements on carbon tows," *EPJ Web of Conferences*, vol. 6, p. 04004, 2010.

[18] P. A. Cundall and O. D. L. Strack, "A discrete numerical model for granular assemblies," *Gotechnique*, vol. 29, no. 1, pp. 47–65, 1979.

[19] B. A. Cheeseman and T. A. Bogetti, "Ballistic impact into fabric and compliant composite laminates," *Composite Structures*, vol. 61, no. 12, pp. 161 – 173, 2003.

[20] C. Lim, V. Shim, and Y. Ng, "Finite-element modeling of the ballistic impact of fabric armor," *International Journal of Impact Engineering*, vol. 28, no. 1, pp. 13 – 31, 2003.

[21] W. Novotny, E. Cepu, A. Shahkarami, R. Vaziri, and A. Poursartip, "Numerical investigation of the ballistic efficiency of multi-ply fabric armours during the early stages of impact," *International Journal of Impact Engineering*, vol. 34, no. 1, pp. 71 – 88, 2007. International Conference on Impact Loading of Lightweight Structures.

[22] G. Nilakantan and J. W. G. Jr., "Ballistic impact modeling of woven fabrics considering yarn strength, friction, projectile impact location, and fabric boundary condition effects," *Composite Structures*, no. 0, pp. –, 2012.

[23] A. Shahkarami and R. Vaziri, "A continuum shell finite element model for impact simulation of woven fabrics," *International Journal of Impact Engineering*, vol. 34, no. 1, pp. 104 – 119, 2007. International Conference on Impact Loading of Lightweight Structures.

[24] R. Barauskas and A. Abraitiene, "Computational analysis of impact of a bullet against the multilayer fabrics in ls-dyna," *International Journal of Impact Engineering*, vol. 34, no. 7, pp. 1286 – 1305, 2007.

[25] G. Nilakantan, M. Keefe, T. A. Bogetti, and J. W. G. Jr., "Multiscale modeling of the impact of textile fabrics based on hybrid element analysis," *International Journal of Impact Engineering*, vol. 37, no. 10, pp. 1056 – 1071, 2010.

[26] M. King, P. Jearanaisilawong, and S. Socrate, "A continuum constitutive model for the mechanical behavior of woven fabrics," *International Journal of Solids and Structures*, vol. 42, no. 13, pp. 3867 – 3896, 2005.

[27] S. D. R. Wilson, "Lateral spreading of fibre tows," *Journal of Engineering Mathematics*, vol. 32, pp. 19–26, 1997.

[28] M. S. Irfan, V. R. Machavaram, R. S. Mahendran, N. Shotton-Gale, C. F. Wait, M. A. Paget, M. Hudson, and G. F. Fernando, "Lateral spreading of a fiber bundle via mechanical means," *Journal of Composite Materials*, vol. 46, no. 3, pp. 311–330, 2012.

[29] H. Bijsterbosch and R. J. Gaymans, "Impregnation of glass rovings with a polyamide melt. part 1: Impregnation bath," *Composites Manufacturing*, vol. 4, no. 2, pp. 85 – 92, 1993.

[30] Y. Wang and X. Sun, "Digital-element simulation of textile processes," *Composites Science and Technology*, vol. 61, no. 2, pp. 311 – 319, 2001.

[31] G. Zhou, X. Sun, and Y. Wang, "Multi-chain digital element analysis in textile mechanics," *Composites Science and Technology*, vol. 64, no. 2, pp. 239 – 244, 2004.

[32] A. Pickett, J. Sirtautas, and A. Erber, "Braiding simulation and prediction of mechanical properties," *Applied Composite Materials*, vol. 16, pp. 345–364, 2009.

[33] Y. Mahadik and S. Hallett, "Finite element modelling of tow geometry in 3d woven fabrics," *Composites Part A: Applied Science and Manufacturing*, vol. 41, no. 9, pp. 1192 – 1200, 2010.

[34] Y. Wang, Y. Miao, D. Swenson, B. A. Cheeseman, C.-F. Yen, and B. LaMattina, "Digital element approach for simulating impact and penetration of textiles," *International Journal of Impact Engineering*, vol. 37, no. 5, pp. 552 – 560, 2010.

[35] H. J. Herrmann, J.-P. Hovi, and S. Luding, "Collisions and contacts between two particles," *Physics of dry granular media*, p. 285, 1998.

[36] M. Lätzel, S. Luding, and H. Herrmann, "Macroscopic material properties from quasi-static, microscopic simulations of a two-dimensional shear-cell," *Granular Matter*, vol. 2, no. 3, pp. 123–135, 2000.

[37] P. W. Cleary and M. Prakash, "Discrete-element modelling and smoothed particle hydrodynamics: Potential in the environmental sciences," *Philosophical Transactions of the Royal Society A: Mathematical, Physical and Engineering Sciences*, vol. 362, no. 1822, pp. 2003–2030, 2004.

[38] J. P. Bardet and J. Proubet, "A numerical investigation of the structure of persistent shear bands in granular media," *Geotechnique*, vol. 41, no. 4, pp. 599–613, 1991.

[39] H. B. Mühlhaus and I. Vardoulakis, "The thickness of shear bands in granular materials," *Géotechnique*, no. 37, pp. 271–283, 1987.

[40] S. Luding, "Constitutive relations for the shear band evolution in granular matter under large strain," *Particuology*, vol. 6, no. 6, pp. 501 – 505, 2008.

[41] K. Iwashita and M. Oda, "Micro-deformation mechanism of shear banding process based on modified distinct element method," *Powder Technology*, vol. 109, no. 1-3, pp. 192 – 205, 2000.

[42] X. Tu and J. Andrade, "Criteria for static equilibrium in particulate mechanics computations," *International Journal for Numerical Methods in Engineering*, vol. 75, no. 13, pp. 1581–1606, 2008.

[43] X. Tu and J. Andrade, "Criteria for static equilibrium in discrete element methods," vol. 10 Part A, pp. 509–516, 2008.

[44] P. A. Cundall, "A discontinuous future for numerical modelling in geomechanics?," *Geotechnical Engineering*, vol. 149, pp. 41–47, 2001.

[45] V. Ogarko and S. Luding, "Equation of state and jamming density for equivalent bi- and polydisperse, smooth, hard sphere systems," *The Journal of Chemical Physics*, vol. 136, no. 12, p. 124508, 2012.

[46] S. Luding, "Liquid-solid transition in bidisperse granulates," *Advances in Complex Systems (ACS)*, vol. 04, no. 04, pp. 379–388, 2001.

[47] S. Luding and O. Strauss, "The Equation of State for Almost Elastic, Smooth, Polydisperse Granular Gases for Arbitrary Density," in *Granular Gases* (T. Pöschel and S. Luding, eds.), Lecture Notes in Physics 564, pp. 389–409, Berlin: Springer, 2000.

[48] D. W. Howell, R. P. Behringer, and C. T. Veje, "Fluctuations in granular media," *Chaos: An Interdisciplinary Journal of Nonlinear Science*, vol. 9, no. 3, pp. 559–572, 1999.

[49] I. Goldhirsch, "Stress, stress asymmetry and couple stress: from discrete particles to continuous fields," *Granular Matter*, vol. 12, pp. 239–252, 2010.

[50] B. Cornelissen, B. Rietman, M. de Rooij, and R. Akkerman, "Tow mechanics: A contact mechanics approach of friction in fibrous tows during forming," *Key Engineering Materials*, vol. Volumes 504 - 506, pp. 325–330.

Appendix A

An optical microscope was used to measure the tow spread at the center spreading bar. The microscope was calibrated with a 20 mm glass plate with divisions of 0.1 mm (fig. A.1). The length per pixel for each zoom was determined using MATLAB and was recorded for later use. The results of the measurements and calculations is shown in table A.1 for different magnifications. For instance for the 4x zoom the length per pixel is 0.00083 mm, which is a very high accuracy. In this case, the required accuracy for measuring the spread is 0.01 mm, which leaves space for an error of more than 10 pixels.
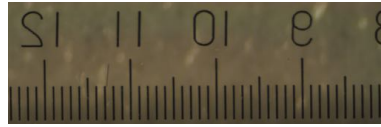

Figure A.1: Glass scale used for calibration and measurement under the microscope using 4x, the distance between the major tick marks is 1.0 mm.

Table A.1: Symbols of particle properties with descriptions

Magnification	Measured length (mm)	Number of pixels	Length (mm) per pixel
0.65	20	3848	0.00520
0.8	17.3	4255	0.00407
1	14	4240	0.00330
1.25	11.3	4283	0.00264
1.6	8.8	4260	0.00207
2	7	4228	0.00166
2.5	5.5	4175	0.00132
3.2	4.3	4155	0.00103
4	3.4	4101	0.00083
4.5	2.8	4235	0.00066

Acknowledgements

A few years back, who would have known that I would graduate at a lovely green university on the edge of the Netherlands. I owe this accomplishment to many people.

First, I would like to thank my supervisor Professor Stefan Luding, who introduced me into the wonderful world of granular materials. His door was always open and he was always able to find a spot for me in his agenda. I may not have understood his instructions at first and agreed with them, but eventually I would see the light. Furthermore, he spent a lot of time reading my thesis, which had a great impact on its final quality.

I also want to thank Professor Remko Akkerman who has been a great contributor on the experimental aspect of the study and for all the advice he provided during the whole course of my study. My sincere gratitude goes out to Bo Cornelissen for the time he dedicated to discuss relevant topics and also reviewing my thesis. I would also like to thank the friendly PhDs, postdocs and staff from the production technology and multiscale mechanics group for making life more pleasant.

There are also other people, who have contributed in other aspects during my studies. Dr. Jelle Ferwerda, the CTW international coordinator, was always there to assist me whenever I required help. I can say for sure that he would go well above his responsibilities and duties to help out international students. It is always comforting to know that there is someone around who is willing to give a helping hand. I am very grateful of the scholarship provided by the University of Twente. I hope that I have been able to contribute to the flow of knowledge at UT during my master studies.

Finally, I save my greatest appreciation to my family members. I cannot neglect the support provided to me by my parents, far far away in Iran, who helped me get where I am now. Surely without their help I would not have made it this far. Last but not least my wife Atefeh, who has parted with her dearest things to stay with me, so we could build our future together.